Cell Reports

Article

Periaxonal and nodal plasticities modulate action potential conduction in the adult mouse brain

Graphical abstract

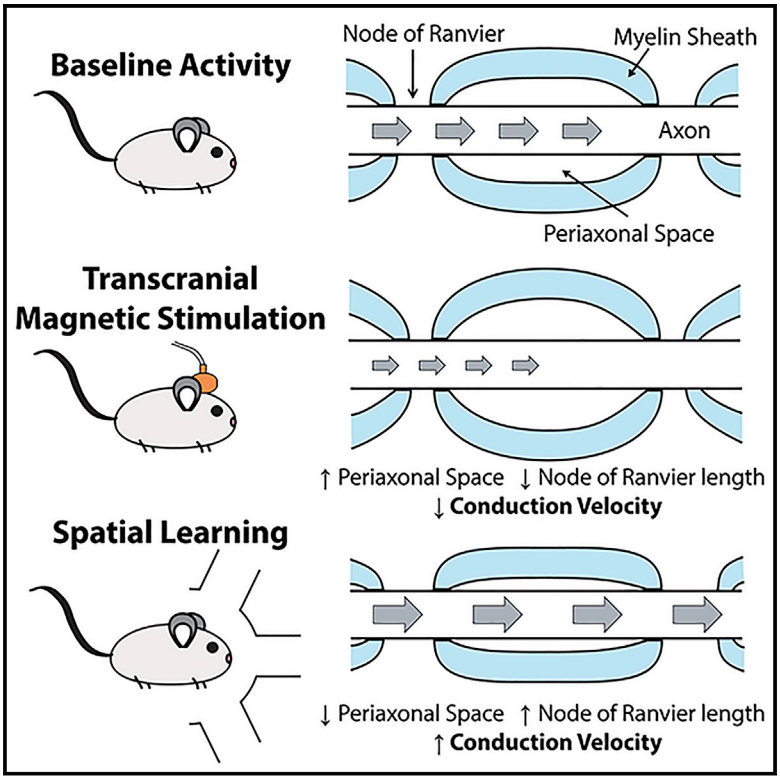

Highlights

- Altering neuronal activity reversibly modifies node of Ranvier length
- Neuronal activity alters periaxonal space width in the adult mouse brain
- Nodal and periaxonal plasticities synergistically modulate action potential speed
- The level of skill acquisition with learning correlates with action potential speed

Authors

Carlie L. Cullen, Renee E. Pepper, Mackenzie T. Clutterbuck, ..., Jennifer Rodger, Renaud B. Jolivet, Kaylene M. Young

Correspondence

kaylene.young@utas.edu.au

In Brief

Cullen et al. show that mature brain cells, called oligodendrocytes, undergo ultrastructural changes during learning. They lengthen the nodes of Ranvier and compress the periaxonal space to speed up action potential conduction. They also report that faster information transfer speeds correlate with greater skill acquisition during learning.

Cullen et al., 2021, Cell Reports *34*, 108641
January 19, 2021
https://doi.org/10.1016/j.celrep.2020.108641

CellPress

Cell Reports

CellPress
OPEN ACCESS

Article

Periaxonal and nodal plasticities modulate action potential conduction in the adult mouse brain

Carlie L. Cullen,[1,8] Renee E. Pepper,[1,8] Mackenzie T. Clutterbuck,[1] Kimberley A. Pitman,[1] Viola Oorschot,[2,7] Loic Auderset,[1] Alexander D. Tang,[3] Georg Ramm,[2] Ben Emery,[4] Jennifer Rodger,[3,5] Renaud B. Jolivet,[6] and Kaylene M. Young[1,9,*]

[1]Menzies Institute for Medical Research, University of Tasmania, Hobart, TAS 7000, Australia
[2]Ramaciotti Centre for Cryo-Electron Microscopy, Monash University, Melbourne, VIC 3800, Australia
[3]Experimental and Regenerative Neuroscience, School of Biological Sciences, University of Western Australia, Perth, WA 6009, Australia
[4]Jungers Center for Neurosciences Research, Department of Neurology, Oregon Health and Science University, Portland, OR 97239-3098, USA
[5]Perron Institute for Neurological and Translational Research, Perth, WA 6009, Australia
[6]Département de Physique Nucléaire et Corpusculaire, University of Geneva, 1211 Geneva 4, Switzerland
[7]Present address: European Molecular Biology Laboratory, Electron Microscopy Core Facility, Heidelberg, Germany
[8]These authors contributed equally
[9]Lead Contact
*Correspondence: kaylene.young@utas.edu.au
https://doi.org/10.1016/j.celrep.2020.108641

SUMMARY

Central nervous system myelination increases action potential conduction velocity. However, it is unclear how myelination is coordinated to ensure the temporally precise arrival of action potentials and facilitate information processing within cortical and associative circuits. Here, we show that myelin sheaths, supported by mature oligodendrocytes, remain plastic in the adult mouse brain and undergo subtle structural modifications to influence action potential conduction velocity. Repetitive transcranial magnetic stimulation and spatial learning, two stimuli that modify neuronal activity, alter the length of the nodes of Ranvier and the size of the periaxonal space within active brain regions. This change in the axon-glial configuration is independent of oligodendrogenesis and robustly alters action potential conduction velocity. Because aptitude in the spatial learning task was found to correlate with action potential conduction velocity in the fimbria-fornix pathway, modifying the axon-glial configuration may be a mechanism that facilitates learning in the adult mouse brain.

INTRODUCTION

Within the central nervous system (CNS), oligodendrocytes (OLs) elaborate myelin internodes to facilitate the rapid and saltatory conduction of action potentials and provide vital trophic support to axons via the periaxonal space (Simons and Nave, 2015). The speed of action potential conduction depends on the molecular and structural parameters of the axon, including its diameter; the presence, length, and thickness of myelin internodes; the length of the nodes of Ranvier; and the relative density of ion channels clustered at the nodes and paranodes (Arancibia-Cárcamo et al., 2017; Ford et al., 2015; Freeman et al., 2016; Halter and Clark, 1993; Seidl, 2014; Young et al., 2013). Axial conduction through the periaxonal space is also important for the saltatory propagation of action potentials (Cohen et al., 2020). These parameters must be carefully controlled, because even seemingly small changes in conduction velocity (CV) have the potential to alter spike-time arrival and prevent input synchrony-dependent facilitation (Zbili et al., 2020). In addition, it has been proposed that CV influences brain wave synchrony (Pajevic et al., 2014). If this is the case, myelination must precisely establish the nodes of Ranvier and the periaxonal space or provide some degree of structural plasticity to this system.

Oligodendrogenesis and myelination commence late in development (Jakovcevski et al., 2009; Kessaris et al., 2006; Lu et al., 2002) and peak before adolescence. However, new OLs are generated throughout life (Dimou et al., 2008; Hill et al., 2018; Hughes et al., 2018; Rivers et al., 2008; Yeung et al., 2014; Young et al., 2013) to replace dying cells (Koenning et al., 2012; Yeung et al., 2014) and add myelin to previously unmyelinated (UM) or partially myelinated axons (Hill et al., 2018). The process of myelination is significantly influenced by experience, because social isolation early in life reduces the addition of myelin to the prefrontal cortex (Liu et al., 2012; Makinodan et al., 2012), and reducing visual input (monocular deprivation) shortens the myelin internodes elaborated by OLs in the affected optic nerve (Etxeberria et al., 2016; Osanai et al., 2018). Conversely, in the adult brain, increasing neuronal activity, either by direct neuronal stimulation or through learning a new skill or task, promotes oligodendrogenesis and myelination of the activated circuits (Cullen et al.,

2019; Gibson et al., 2014; Li et al., 2010; McKenzie et al., 2014; Mitew et al., 2018; Sampaio-Baptista et al., 2013; Steadman et al., 2020).

In the developing zebrafish spinal cord, the extension and retraction of internodes is regulated by distinct patterns of calcium activity within the nascent myelin sheaths, and this can be partially regulated by neuronal activity (Baraban et al., 2018; Krasnow et al., 2018). In the mammalian brain, periodic and mitochondria-derived calcium transients can be detected within myelin sheaths that increase in frequency at the peak of cortical myelination and during remyelination in the adult mouse brain (Battefeld et al., 2019). Even after maturation, OLs retain some capacity for internode remodeling, with a subset of internodes extending or retracting over time (Hill et al., 2018; Hughes et al., 2018). This capacity is perhaps best highlighted by the extension of established myelin sheaths to occupy an adjacent segment of recently demyelinated axon, following the ablation of a single myelinating OL in the zebrafish spinal cord (Auer et al., 2018). However, the extent to which mature OLs remodel their internodes in the healthy brain, in response to specific physiological stimuli such as altered neuronal activity, has not been explored.

Herein, we show that modulating neuronal activity, either artificially by delivering low-intensity repetitive transcranial magnetic stimulation (LI-rTMS) or physiologically through learning, has no net effect on gross internode length but induces adaptive changes to the axo-myelinic ultrastructure to alter action potential CV in the adult mouse brain. Because the performance of individual mice in the spatial learning radial arm maze (RAM) task correlated with CV along myelinated (M) fimbria-fornix axons, these ultrastructural changes may facilitate learning.

RESULTS

The gross myelinating morphology of mature OLs does not change with iTBS

We have previously shown that non-invasive LI-rTMS, delivered in an intermittent theta burst stimulation (iTBS) pattern, promotes the survival and maturation of new OLs within the primary motor cortex (M1) (Cullen et al., 2019). To determine whether the non-invasive stimulation of M1 could induce adaptive changes in myelinating OLs, we labeled a subset of mature cortical OLs by giving a single dose of tamoxifen to adult (postnatal day [P] 83) *Plp-CreER::Tau-mGFP* transgenic mice one week before commencing LI-rTMS (see STAR Methods). Following 14 days of sham stimulation or iTBS, we analyzed the morphology of myelinating OLs within M1 (Figures 1A and 1B) and the underlying corpus callosum (CC) (Figures 1C and 1D) that were labelled with a membrane-targeted form of green fluorescent protein (mGFP). More specifically, we measured the length of mGFP$^+$ internodes that were flanked on each end by contactin-associated protein (CASPR)$^+$ paranodes (Figures 1C and 1D). We found that internodes elaborated by pre-existing mGFP$^+$ M1 OLs were shorter (~5–118 μm, range; 30.28 ± 0.77, mean ± SD) (Figures 1E and 1F) than those elaborated in CC (~10–104 μm, range; 50.68 ± 1.02, mean ± SD) (Figures 1G and 1H) but that iTBS did not alter the average length (Figures 1F and 1H) or length distribution (Figures 1E and 1G) of internodes in either region. The density of mGFP$^+$ internodes within CC (Figure S1) made it impossible to attribute internodes to any single cell within this region. However, we were able to determine the number of internodes maintained by individual OLs within M1 and found that this was also unchanged by iTBS (sham: 29 ± 3, iTBS: 28 ± 2, mean ± SEM; t test, $p = 0.62$; $n = 13$ and 12 cells, respectively), indicating that iTBS does not lead to detectable changes in the gross myelinating morphology of mature OLs.

iTBS shortens nodes of Ranvier

At the end of each internode, anchoring proteins expressed by the myelin loops, such as neurofascin 155, interact with the axonal proteins contactin and CASPR to form paranodes (Bhat et al., 2001; Charles et al., 2002; Klingseisen et al., 2019; Peles et al., 1997; Sherman et al., 2005). These paranodal junctions maintain voltage-gated sodium channels ($Na_v1.6$) at the nodes of Ranvier (Freeman et al., 2015, 2016; Suzuki et al., 2004). It has been suggested that node length is plastic and may change in response to altered neuronal activity to fine-tune action potential propagation in accordance with information processing needs (Arancibia-Cárcamo et al., 2017; Ford et al., 2015); however, this has not yet been confirmed experimentally.

To determine whether iTBS affects specific axonal domains, we immunolabeled coronal brain sections from iTBS and sham-stimulated animals to visualize paranodes (CASPR) and nodes of Ranvier ($Na_v1.6$) (Figures 2A–2D). By identifying regions of dense $Na_v1.6$ staining that were clearly flanked by abutting CASPR$^+$ paranodes, we quantified the length of individual nodes within M1 (Figures 2A, 2B, and 2E) and the underlying CC (Figures 2C, 2D, and 2F). We found that 14 days of iTBS treatment shifted node length distribution toward shorter nodes within both M1 (Figure 2E) and CC (Figure 2G), which corresponded to an ~19% reduction in average node length in M1 (Figure 2F) and an ~16% decrease in CC (Figure 2H). Nodal shortening was not accompanied by a change in paranode length (or length distribution) (Figures S2A–S2D). To confirm the effect of iTBS on node length, we also performed high-resolution stimulated emission depletion (STED) microscopy to visualize callosal nodes ($Na_v1.6$) and paranodes (CASPR) in a separate cohort of animals following 14 days of iTBS or sham stimulation (Figures S2E and S2F). Consistent with our initial observations, we found that iTBS shifted the node length distribution toward shorter nodes (Figure S2G), which corresponded to a reduction of ~18% in average node length per mouse within CC (Figure S2H).

To evaluate the impact of treatment duration on node length, we compared the effect of delivering a sham stimulation or iTBS for 7, 14, or 28 days (Figure S2). 7 days of iTBS was insufficient to alter average node length in M1 (Figure S2I) or CC (Figure S2J). By contrast, 28 days of iTBS shortened average node length by ~19% in M1 (Figure S2I) and ~18% in CC (Figure S2J), which is equivalent to 14 days of stimulation. Therefore, in response to iTBS, nodes shorten and then remain short while stimulation is maintained. To determine whether ceasing iTBS results in node length reverting to that measured in sham-stimulated mice, we delivered 14 days of sham or iTBS and then ceased stimulation for 7 days (14+7 days) before measuring the length of individual nodes. At this time point, the average

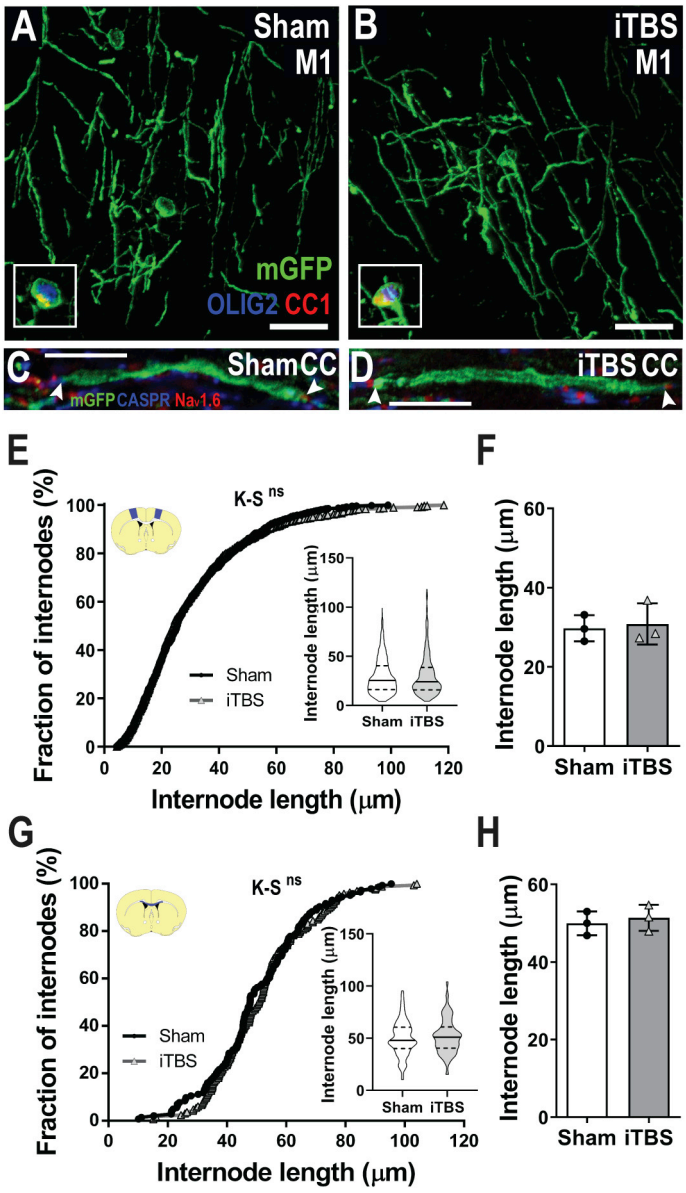

Figure 1. iTBS does not alter OL gross myelinating morphology

(A and B) Compressed confocal z stack of a mGFP$^+$ (green) OL in the primary motor cortex (M1) of *Plp-CreER::Tau-mGFP* transgenic mice after 14 days of sham stimulation (A) or iTBS (B). Inset, mGFP$^+$ cell bodies show co-labeling for CC1 (red) and OLIG2 (blue).

(C and D) Single mGFP$^+$ internodes flanked on either end by CASPR$^+$ paranodes (blue) and dense $Na_v1.6$ staining at the node of Ranvier (red) in the corpus callosum (CC) of sham-stimulated mice (C) or iTBS mice (D).

(E and F) Cumulative M1 mGFP$^+$ internode length distribution for sham (black circles) and iTBS (gray triangles) mice (E) (744 sham internodes; 733 iTBS internodes; Kolmogorov-Smirnov [K-S] test, K-S D = 0.049, p = 0.32; inset violin plot of internode length, Mann-Whitney U [MWU] test, p = 0.63) and the average M1 internode length per sham (white bars) and iTBS (gray bars) mouse (F) (n = 3 mice per group; t test, t = 0.31, p = 0.77).

(G and H) Cumulative CC mGFP$^+$ internode length distribution (G) (n = 144 sham internodes; n = 166 iTBS internodes; K-S test, K-S D = 0.08, p = 0.63; inset violin plot of internode length, MWU test, p = 0.57) and average CC internode length per sham and iTBS mouse (H) (n = 3 mice per group; t test, t = 0.55, p = 0.61).

Arrowheads indicate the end of an internode. Violin plots show the median (solid line) and interquartile range (dashed lines). Bars show mean ± SD. Scale bars represent 20 μm.

See also Figure S1.

length and length distribution of M1 nodes was equivalent in sham and iTBS mice (Figures 2I and 2J), suggesting that this form of plasticity is reversible. Within CC of 14+7 day iTBS mice, node length distribution remained significantly shifted toward shorter nodes (Figure 2K), corresponding to an ~20% decrease in average node length (Figure 2L), perhaps suggesting that nodal changes are more long-lived in the white matter.

Spatial learning lengthens nodes of Ranvier

Learning physiologically modulates neuronal activity (Benchenane et al., 2010; Dupret et al., 2010, 2013; Negrón-Oyarzo et al., 2018). Spatial learning enhances activity within the hippocampal-cortical network and is accompanied by an increase in OL addition to this network (Steadman et al., 2020), whereas motor learning is accompanied by a similar increase in oligodendrogenesis and myelination in CC (Sampaio-Baptista et al., 2013; Xiao et al., 2016). To explore the possibility that mature OLs also respond to learning (L), we administered tamoxifen to P60 *Plp-CreER::Tau-mGFP* transgenic mice and then trained these mice (from P74) to learn a hippocampal-dependent RAM task (STAR Methods; Figures S3A and S3C). The subset of *Plp-CreER::Tau-mGFP* transgenic mice exposed to the maze, but not trained to learn the location of food rewards, are called no-learning (NL) controls (Figure S3B). Following 14 days of NL or L, we analyzed the morphology of mGFP-labeled myelinating OLs within the hippocampal fimbria (Figures 3A and 3B), a major white matter tract that connects both hippocampi with subcortical and cortical regions, including the thalamus and prefrontal cortex (Jin and Maren, 2015; Wyss et al., 1980). Because of the density of mGFP$^+$ internodes within the fimbria (Figure S1C), it was not possible to reliably attribute internodes to a single cell; however, by measuring the length of individual mGFP$^+$ internodes, flanked by CASPR$^+$ paranodes (Figure 3C), we determined that internodes within the fimbria were ~5–109 μm in length (inset, Figure 3D) and that spatial learning had no effect on the average length or length distribution of internodes in this region (Figures 3D and 3E).

To determine whether RAM learning induced nodal plasticity, we quantified the length of nodes ($Na_v1.6$) and paranodes (CASPR) (Figures 3F and 3G) within the fimbria of NL and L mice. Unlike iTBS, which shortened nodes, spatial learning produced a shift in node length distribution toward longer nodes (Figure 3H) and produced a corresponding ~16% increase in average node length (Figure 3I). However, like iTBS, spatial learning did not alter the average length or length distribution of paranodes (Figures S3D and S3E).

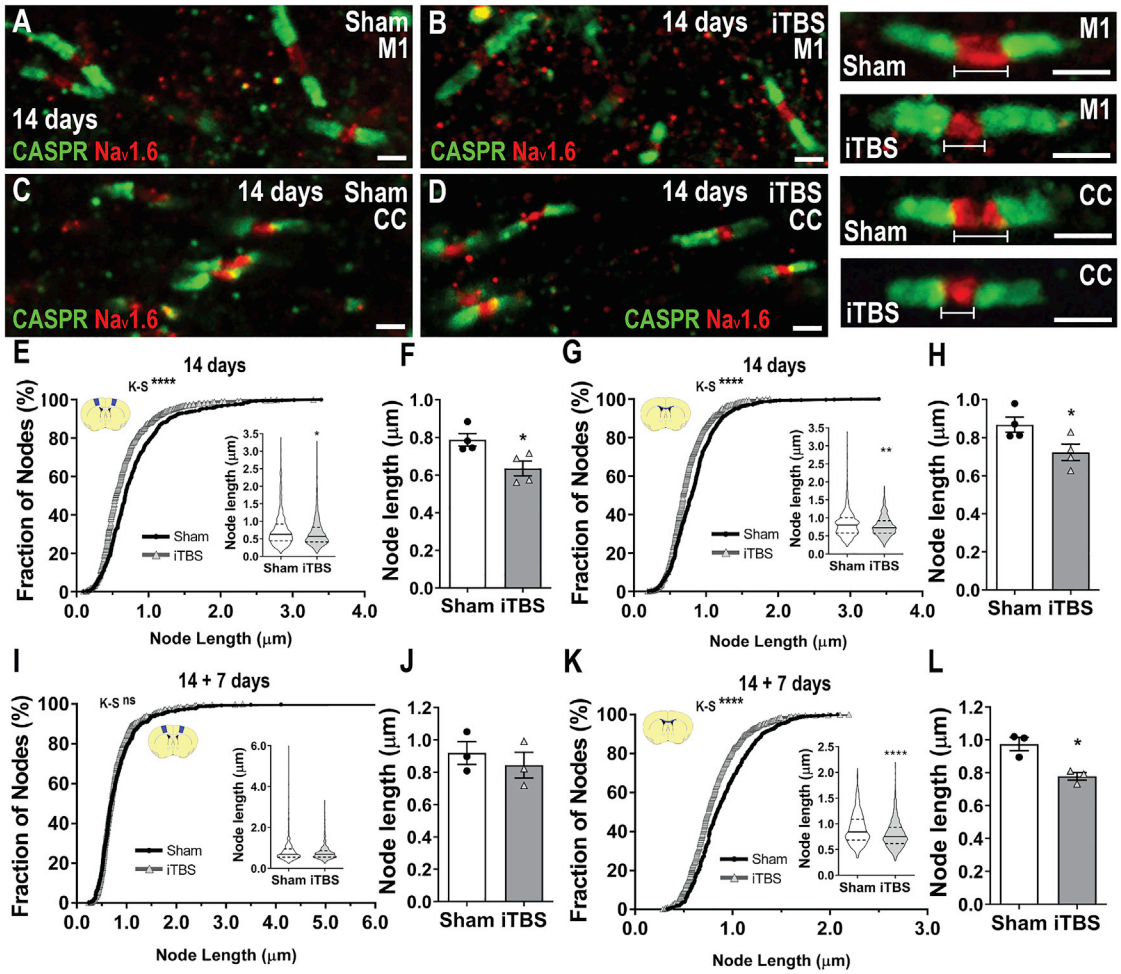

Figure 2. iTBS shortens nodes of Ranvier

(A–D) Confocal images of nodes of Ranvier ($Na_v1.6$; red) and paranodes (CASPR; green) in M1 (A and B) and CC (C and D) after 14 days of sham stimulation or iTBS.

(E and F) Cumulative M1 node length distribution (656 sham nodes, black circles; 802 iTBS nodes, gray triangles; K-S test, K-S D = 0.19, $p < 0.0001$; inset: violin plot of node length, MWU test, $p < 0.0001$) and average M1 node length per sham (white bars) and iTBS (gray bars) mouse (F) (n = 4 mice per group; t test, t = 2.95, p = 0.02).

(G and H) Cumulative CC node length distribution (G) (867 sham nodes; 700 iTBS nodes; K-S D = 0.13, $p < 0.0001$; inset: violin plot of node length, MWU test, $p < 0.0001$) and average CC node length per sham and iTBS mouse (H) (n = 4 mice per group; t test, t = 2.50, p = 0.04).

(I and J) Cumulative M1 node length distribution (I) (452 sham nodes; 576 iTBS nodes; K-S D = 0.070, p = 0.15; inset: violin plot of node length, MWU test, p = 0.35) and average M1 node length per sham and iTBS mouse (J) (n = 3 per group; t test, t = 0.70, p = 0.52) 7 days after cessation of stimulation (14+7 days).

(K and L) Cumulative CC node length distribution (K) (587 sham nodes; 696 iTBS nodes; K-S D = 0.16, $p < 0.0001$; inset: violin plot of node length, MWU test, $p < 0.0001$) and average CC node length per sham and iTBS-treated mouse (L) (n = 3 per group; t test, t = 4.2, p = 0.01) 7 days after cessation of stimulation (14+7 days).

*$p < 0.05$, ****$p < 0.0001$. Violin plots show the median (solid line) and interquartile range (dashed lines). Bars show mean ± SD. Scale bars represent 1 μm. See also Figure S2.

Nodal plasticity does not require adult oligodendrogenesis

The addition of new OLs can influence node length in the adult mouse brain (Schneider et al., 2016), and the administration of tamoxifen to P60 *Pdgfrα-CreER^{TM}::Rosa26-YFP* mice, to allow lineage tracing of oligodendrocyte progenitor cells (OPCs) during RAM training, revealed that RAM learning increases the number of new OLs detected in the fimbria (NL: 76 ± 4 YFP^+ PDGFRα--neg $OLIG2^+$ OLs/mm^2, L: 115 ± 23 YFP^+ PDGFRα-neg $OLIG2^+$ OLs/mm^2 [mean of n = 3 mice per group ± SD]; two-tailed unpaired t test, t = 2.78, df = 4, p = 0.04). Because previous reports indicate that preventing adult oligodendrogenesis simultaneously lengthens nodes and their flanking paranodes (Schneider et al., 2016), RAM learning, which increases oligodendrogenesis, should shorten nodes and paranodes. Instead, RAM learning lengthened the nodes of Ranvier and had no effect on paranode length, suggesting that adult oligodendrogenesis cannot account for nodal plasticity in this context.

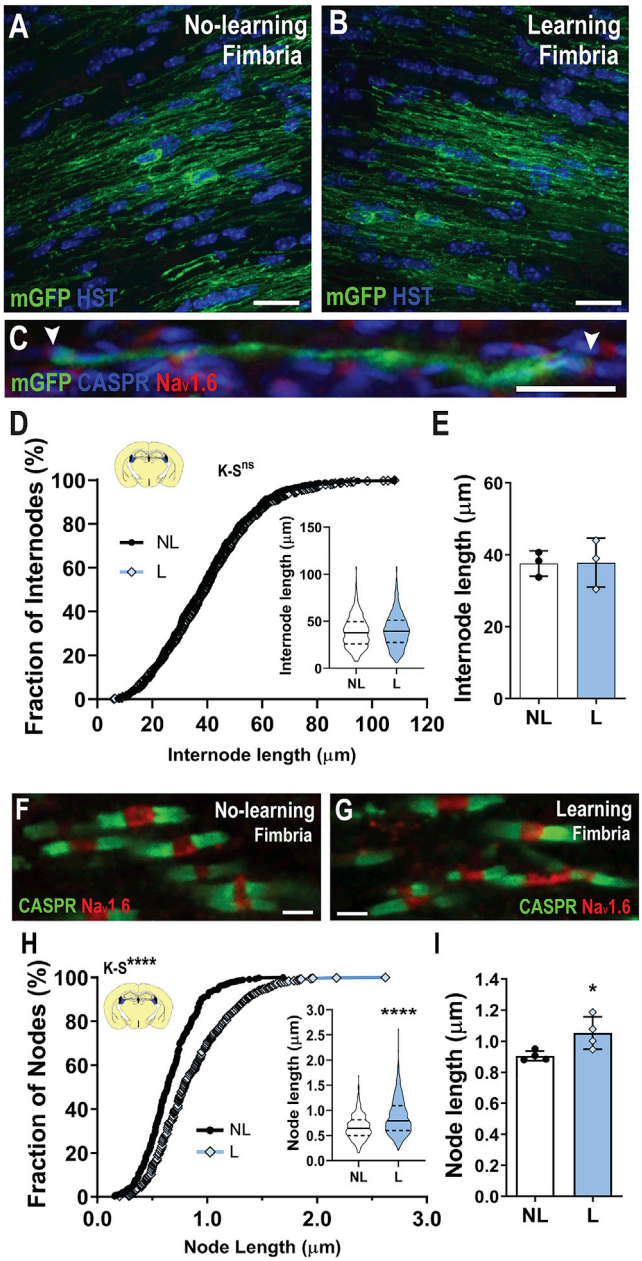

Figure 3. Spatial learning lengthens nodes of Ranvier

(A and B) Compressed confocal z stack of a mGFP$^+$ (green) OLs in the hippocampal fimbria of *Plp-CreER::Tau-mGFP* transgenic mice after 14 days of no-learning (NL) (A) or learning (L) (B) in the radial arm maze.

(C) Example of a single mGFP$^+$ fimbria internode flanked on either end by CASPR$^+$ paranodes (blue) and dense $Na_v1.6$ staining (red) at the node of Ranvier.

(D and E) Cumulative internode length distribution for mGFP$^+$ internodes of NL (black circles) and L (blue diamonds) mice (D) (n = 532 NL; n = 685 L; K-S test, K-S D = 0.054, p = 0.34; inset: violin plot of internode length, MWU test, p = 0.15) and average fimbria internode length per animal (E) in NL mice (white bars) and L mice (blue bars) (n = 3 mice per group; t test, t = 0.053, p = 0.96).

(F and G) Confocal images of nodes of Ranvier ($Na_v1.6$; red) and paranodes (CASPR; green) in the fimbria of NL mice (F) and L mice (G).

(H and I) Cumulative node length distribution in the fimbria (H) (448 NL nodes; 520 L nodes; K-S D = 0.25, p < 0.0001; inset: violin plot of node length, MWU test, p < 0.0001) and average fimbria node length per animal (I) in NL and L mice (n = 4 per group; t test, t = 2.72, p = 0.03).

*p < 0.05, ****p < 0.0001. Violin plots show the median (solid line) and interquartile range (dashed lines). Bars show mean ± SD. Scale bars represent 15 μm (A–C) and 1 μm (F and G).

See also Figures S1 and S3.

To determine whether nodal plasticity can occur in the absence of oligodendrogenesis, tamoxifen was administered to P76 *Pdgfrα-CreER^{TM}::Rosa26-YFP::Myrf$^{fl/fl}$* (Myrf$^{fl/fl}$) mice to fluorescently label OPCs and conditionally delete myelin regulatory factor (*Myrf*), a transcription factor essential for OL maturation and myelin maintenance (Emery et al., 2009). The conditional deletion of *Myrf* from adult OPCs reduced OL addition in M1 ($p < 0.05$) and CC ($p < 0.001$) by >60% within 30 days of tamoxifen delivery (Figures S4A–S4F). However, when sham stimulation or iTBS was initiated 14 days after tamoxifen delivery (P76+14) and the nodes of Ranvier ($Na_v1.6$) were imaged in M1 at P76+28 (Figures S4G and S4H), iTBS again shifted the node length distribution toward shorter nodes (Figure S4I, K-S test, $p < 0.0001$) and decreased the average node length by ~16% (Figure S4J, t test, p = 0.04). Within CC of Myrf$^{fl/fl}$ mice, iTBS also shortened nodes (Figure S4K, K-S test, $p < 0.0001$; Figure S4L, t test, p = 0.01). Similarly, when P60+14 Myrf$^{fl/fl}$ mice underwent 14 days of RAM training, length distribution of the node of Ranvier ($Na_v1.6$) was again shifted toward longer nodes in mice that learned (L mice) compared with those that did not (NL controls) (Figures S4M–S4O, K-S test, $p < 0.0001$), and this corresponded to an ~24% increase in average node length (Figure S4P, t test, p = 0.004). These data indicate that the nodal plasticity induced by iTBS or spatial learning cannot be entirely attributed to new OL addition.

To explore the possibility that nodal plasticity is instead mediated by mature, pre-existing OLs, we used *Plp-CreER::Tau-mGFP* transgenic mice to selectively identify nodes of Ranvier ($Na_v1.6$) that were already formed before iTBS or sham stimulation. These nodes were identified as being flanked by mGFP$^+$ pre-existing internodes (Figures 4A and 4B). Within M1, iTBS shortened the mature nodes (Figure 4C) and tended to decrease the average length of the mature nodes in each mouse by ~18% (Figure 4D, p = 0.056). Within CC, iTBS also shifted mature node length distribution toward shorter nodes (Figure 4E), which corresponded to an ~23% decrease in average node length (Figure 4F), suggesting that node shortening is facilitated by mature OLs.

To determine whether the node lengthening induced by spatial learning is also facilitated by mature OLs, we similarly analyzed nodes flanked by mGFP$^+$ pre-existing internodes in the fimbria of NL (Figure 4G) and L (Figure 4H) *Plp-CreER::Tau-mGFP* transgenic mice. Consistent with our earlier observations, learning shifted the length distribution of mature nodes toward longer nodes (Figure 4I) and increased the average length of mature nodes by ~17% (Figure 4J, p = 0.051). These data suggest that mature OLs facilitate activity-induced nodal plasticity through the subtle expansion or retraction of existing myelin internodes.

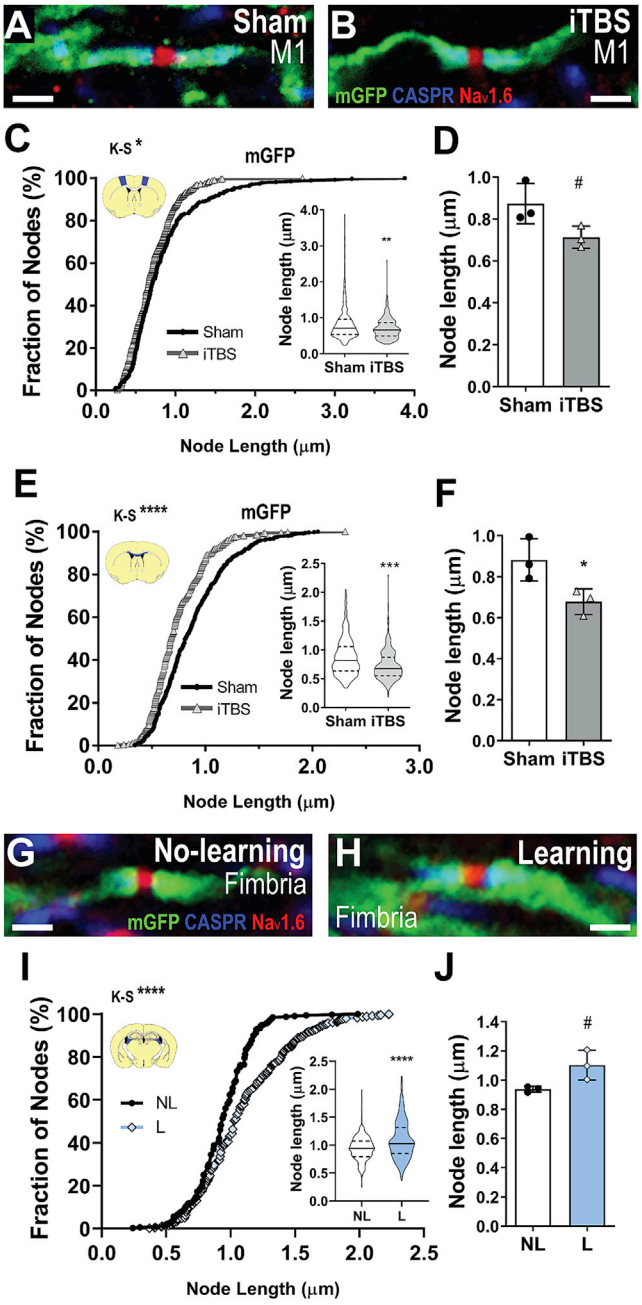

Figure 4. Nodes between mature internodes are plastic

(A and B) Mature node of Ranvier ($Na_v1.6$; red) flanked by CASPR$^+$ paranodes (blue) and mGFP$^+$ internodes (green) in M1 of *Plp-CreER::Tau-mGFP* mice following sham treatment (A) or iTBS treatment (B).

(C and D) Cumulative mature node length distribution in M1 (C) (273 sham mature nodes, black circles; 325 iTBS mature nodes, gray triangles; K-S D = 0.11, p = 0.03; inset: violin plot of node length, MWU test, p = 0.0019) and average mature M1 node length per sham (white bars) and iTBS (gray bars) animal (D) (n = 3 per group; t test, t = 2.52, p = 0.056).

(E and F) Cumulative mature node length distribution in CC (E) (495 sham mature nodes; 435 iTBS mature nodes; K-S D = 0.22, p < 0.0001; inset: violin plot of node length, MWU test, p < 0.0001) and average mature M1 node length per individual sham-stimulated and iTBS mouse (F) (n = 3 per group; t test, t = 2.94, p = 0.04).

(G and H) Mature node of Ranvier ($Na_v1.6$; red) flanked by CASPR$^+$ paranodes (blue) and mGFP$^+$ internodes (green) in the fimbria of *Plp-CreER::Tau-mGFP* in mice that underwent NL (G) or L (H) in the RAM.

(I and J) Cumulative mature node length distribution in the fimbria (I) (319 NL mature nodes, black circles; 453 L mature nodes, blue diamonds; K-S D = 0.25, p < 0.0001; inset: violin plot of node length, MWU test, p < 0.0001) and average mature node length per individual NL (white bars) and L (blue bars) mouse (J) (n = 3 per group; t test, t = 2.75, p = 0.051).

#p < 0.06, *p < 0.05, **p < 0.01, ***p < 0.001, ****p < 0.0001. Violin plots show the median (solid line) and interquartile range (dashed lines). Bars show mean ± SD. Scale bars represent 1 μm.

See also Figure S4.

iTBS and spatial learning alter the size of the periaxonal space

For internodes to encroach on or retract from the nodes of Ranvier, the thickness or structure of myelin must be modified. For example, the sustained activation of extracellular signal-regulated kinases 1 and 2 (ERK1/2) in mature OLs induces a marked decrease in node length in CC of adult mice by increasing myelin thickness (Jeffries et al., 2016), and in the optic nerve, the thrombin-dependent detachment of paranodal loops leads to thinner myelin (fewer myelin wraps) and longer nodes (Dutta et al., 2018). Therefore, we performed transmission electron microscopy (TEM) to quantify the g-ratio [axon diameter/(axon + myelin sheath diameter)] of M axons in CC of adult sham and iTBS-treated mice (Figures 5A–5K). We found that iTBS resulted in a shift in the distribution of axonal g-ratio measurements toward smaller values (Figures 5C and 5E), which corresponded to an ~7% reduction in the average g-ratio measured for M axons in iTBS mice compared with controls (Figure 5D).

Because axon diameter was similar between treatment groups (iTBS: 0.53 ± 0.17 μm, sham: 0.58 ± 0.16 μm; t test, p = 0.09), the decreased g-ratio could reflect an increase in myelin thickness; however, when we quantified the number of myelin wraps (lamellae) around individual axons in the CC, we found that the number of myelin wraps was not affected by treatment (Figures 5D–5I). Similarly, the average thickness (periodicity) of each wrap (the distance between each major dense line) (capped lines in Figures 5E and 5G) (sham: 8.3 ± 0.3 nm, iTBS: 8.6 ± 0.2 nm, mean ± SD; n = 3 per group; t test, t = 1.27, p = 0.27) and the cross-sectional area of the inner tongue process (sham: 11,287 ± 2,266 nm^2, iTBS: 13,124 ± 3,179 nm^2, mean ± SD; n = 3 per group; t test, t = 0.81, p = 0.46) were unchanged by iTBS. However, the width of the fluid-filled space that exists between the axon and the internode, known as the periaxonal space, increased by ~47% following iTBS (Figures 5J and 5K), perhaps suggesting that the myelin sheath is pushed outward or reconfigured away from the axon. This was not the result of a generalized or widespread change in ion balance and osmosis resulting from iTBS, because no effect was seen on the size of M1 neuronal somata (NEUN$^+$ MAP2$^+$; sham-stimulated: 150.4 ± 8.6 μm^2, iTBS: 150.6 ± 7.6 μm^2, mean ± SD; n = 4 mice per group; t test, t = 0.04, df = 6, p = 0.96) or callosal OL somata (mGFP$^+$; sham-stimulated: 38.5 ± 2.2 μm^2, iTBS: 38.1 ± 3.7 μm^2, mean ± SD; n = 3 mice per group; t test, t = 0.15, df = 4, p = 0.88).

Remarkably, spatial learning had the opposite effect on myelin ultrastructure in the fimbria (Figures 5L–5T). Learning produced a

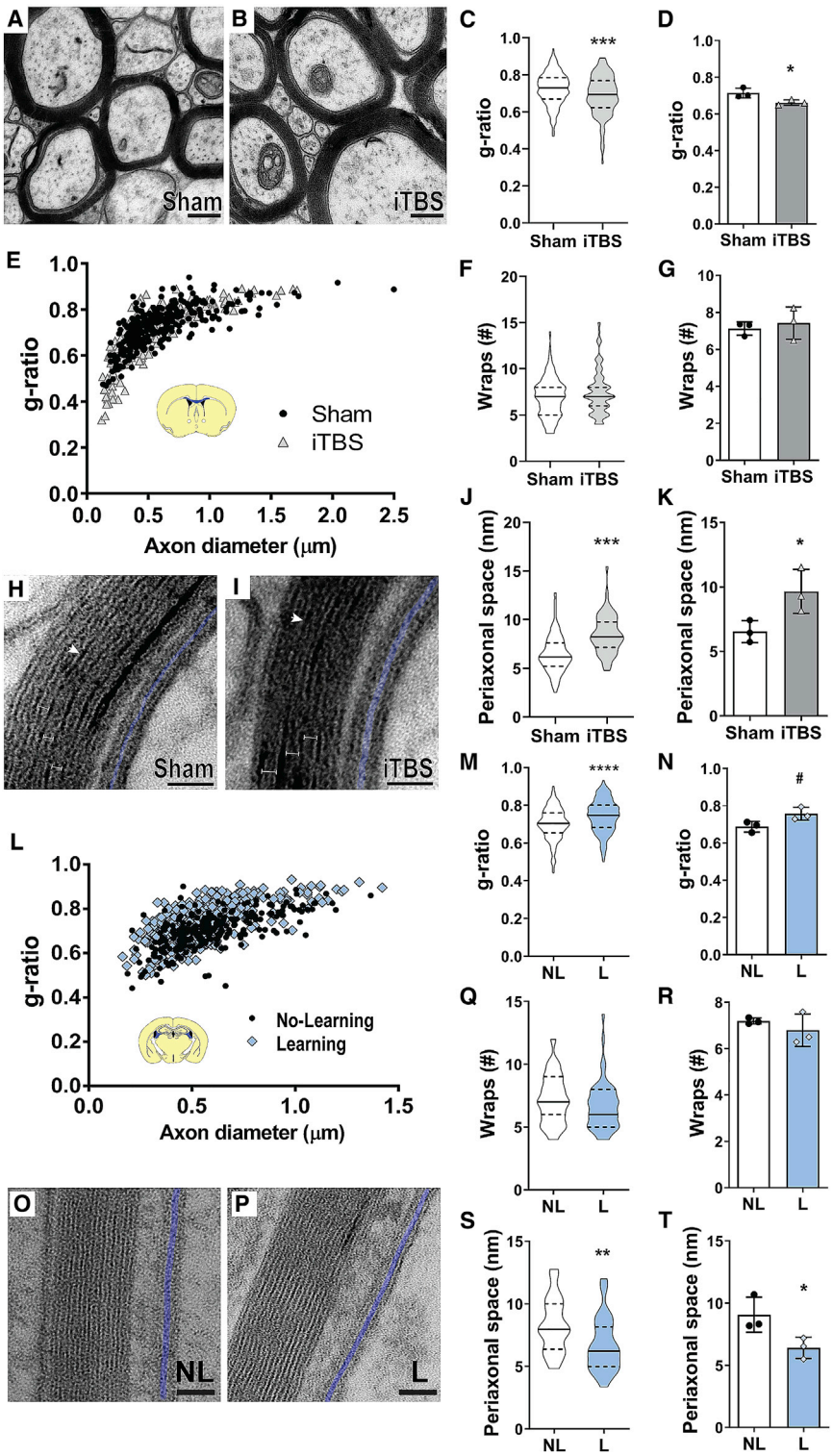

Figure 5. iTBS and spatial learning alter the size of the periaxonal space

(A and B) TEM images of axons within CC of a sham-stimulated mouse (A) and iTBS mouse (B).

(C) Violin plot of g-ratio (323 sham axons, white; 301 iTBS axons, gray; MWU test, $p < 0.0001$).

(D) Average g-ratio per individual sham and iTBS animal (t test, $t = 2.98$, $p = 0.04$).

(E) Axonal diameter versus g-ratio for axons in CC of sham-stimulated (black circles; n = 323 axons) and iTBS (gray triangles; n = 301 axons) mice (K-S test for g-ratio, K-S D = 0.18, $p < 0.0001$).

(F) Violin plot of the number of myelin wraps per axon (104 sham axons; 125 iTBS axons; MWU test, $p = 0.23$).

(G) Average number of myelin wraps per individual sham and iTBS animal (t test, $t = 0.54$, $p = 0.61$).

(H and I) High-magnification TEM image of a myelinated (M) axon in CC of a sham-stimulated mouse (H) and iTBS mouse (I). White arrows, major dense line. Blue shading, periaxonal space.

(J) Violin plot of periaxonal space width (75 sham axons; 60 iTBS axons; MWU test, $p < 0.0001$).

(K) Average periaxonal space width per individual sham and iTBS animal (t test, $t = 2.84$, $p = 0.04$).

(L) Axon diameter versus g-ratio for axons in the fimbria of NL (black circles) or L (blue diamonds) mice (209 NL axons; 374 L axons; K-S test for g-ratio, K-S D = 0.24, $p < 0.0001$).

(M) Violin plot of g-ratio (209 NL axons, white; 374 L axons, blue; MWU test, $p < 0.0001$).

(N) Average g-ratio per individual NL and L animal (t test, $t = 2.64$, $p = 0.057$).

(O and P) TEM image of a M axon in the fimbria of a NL mouse (O) and L mouse (P).

(Q) Violin plot of the number of myelin wraps per axon (55 NL axons; 55 L axons; MWU test, $p = 0.10$).

(R) Average number of myelin wraps per individual NL and L animal (t test, $t = 0.98$, $p = 0.38$).

(S) Violin plots of periaxonal space width (36 NL axons; 38 L axons; MWU test, $p = 0.0023$).

(T) Average periaxonal space width per individual NL and L animal (t test, $t = 2.78$, $p = 0.04$).

Capped lines, single myelin wrap. $^{\#}p < 0.06$, $^{*}p < 0.05$, $^{**}p < 0.01$, $^{***}p < 0.001$, $^{****}p < 0.0001$. Violin plots show the median (solid line) and interquartile range (dashed lines). Bars show mean ± SD for n = 3 animals per group. Scale bars represent 200 nm (A and B), 25 nm (H and I), or 50 nm (O and P).

significant shift toward larger g-ratio values for M axons in the fimbria (Figures 5L and 5M), which corresponded to an ~9% increase in the average g-ratio (Figure 5N, $p = 0.057$). This increase in g-ratio could not be explained by a change in axon diameter (NL: 0.61 ± 0.01 μm, L: 0.56 ± 0.11 μm, mean ± SD; n = 3 per group; t test, $t = 0.87$, $p = 0.42$) or the number of myelin wraps elaborated (Figures 5O–5R), but it was associated with an ~29% decrease in the average width of the periaxonal space (Figures 5S and 5T). These data suggest that modulating neuronal activity can induce adaptive changes in myelin ultrastructure to alter the length of the node of Ranvier and the width of the periaxonal space, two of the axon-glial parameters that strongly influence action potential CV.

The size of the periaxonal space modulates CV

The frequency and composition of nodal domains can markedly affect action potential propagation along an axon (Ford et al., 2015; Freeman et al., 2016; Schneider et al., 2016), and node length is predicted to exert a strong influence on CV (Arancibia-Cárcamo et al., 2017; Halter and Clark, 1993). Within the rat cortex, the estimated density of $Na_v1.6$ channels at the node is relatively stable across nodes of various lengths, and this constant density of ion channels was predicted to ensure a concave relationship between node length and speed of conduction, such that increasing node length increased CV to a point, after which very long nodes (like very short nodes) caused a reduction in CV (Arancibia-Cárcamo et al., 2017). Furthermore, the inclusion or omission of periaxonal space width could result in new internodes increasing or decreasing the simulated CV of an axon, respectively (Young et al., 2013). More recently, it was reported that electrical conductance within the periaxonal space facilitates the saltatory propagation of action potentials and that changing the size of this space would theoretically alter CV (Cohen et al., 2020).

To determine how changes in node length and periaxonal ultrastructure might influence CV, we performed computational simulations of action potential propagation in M callosal axons by adapting the mathematical model developed by Richardson and colleagues (Bakiri et al., 2011; Richardson et al., 2000) (Figures 6A and 6B; see STAR Methods and Figure S5). We initially explored how the size of the periaxonal space might affect CV (Figures 6C and 6D), and in line with Cohen et al. (2020), we found that simulated CV is up to 3.5 times slower when the periaxonal space width is set to 20 nm rather than 0 nm (Figure 6C), which equates to a conduction delay of up to ~9 ms (at 21°C) over a distance of 1 cm (Figure 6D).

By initially configuring the model parameters so that the periaxonal space was uniform under the internode and paranode (Figure 6E) and setting all other parameters to match those measured under sham conditions (Figure 6F; Table S1), we obtained a theoretical CV of 1.18 m/s at 21°C (1.91 m/s at 37°C) (Figure S5). Reducing the node length to that measured after iTBS (Figure 2; Table S1) slowed action potential propagation by ~2.3%, whereas altering the myelin sheath parameters (measured increase in periaxonal space and associated decrease in g-ratio = altered myelin) (Figure 5; Table S1) exerted a greater influence on CV, effectively slowing propagation by ~8.6% (Figure 6F). We found that modifying both sets of parameters—i.e., reducing node length and increasing the periaxonal space width (altered myelin) to reflect the ultrastructural changes observed following iTBS (Figures 2 and 5; Table S1)—had an additive effect, slowing CV by ~10.9% (to 1.05 m/s) (Figure 6F). This effect was exaggerated at 37°C, with iTBS inducing a theoretical ~12.3% reduction in CV (Figure S5D).

We then changed the model parameters so that the periaxonal space under the internode could change but did not exceed 3 nm at the paranode (Figure 6G), which is the middle of the size range that has been reported elsewhere (Nans et al., 2011; Rosenbluth, 1995; Waxman et al., 1995). In this scenario, the simulated CV for sham-stimulated axons was slightly faster: 1.34 m/s at 21°C (Figure 6H; 37°C data in Figure S5F). Reducing node length still slowed CV by ~2.3%, but the effect of altering the periaxonal space (altered myelin) was diminished, slowing conduction by only ~3.7%, such that the combined effect of reduced node length + altered myelin (iTBS) was also weaker, inducing a theoretical ~6% reduction in CV (Figure 6H; ~5.7% reduction at 37°C in Figure S5F). In a third model, we simulated a scenario in which the periaxonal space was narrower, by half, at the paranode but changed proportionally with the internodal periaxonal space (Figure 6I). In this scenario, the simulated CV using sham parameters was 1.32 m/s (Figure 6J) at 21°C (37°C data in Figure S5H), but the reduction in CV induced by altering the periaxonal space width (altered myelin; ~9.2%) or by mimicking the iTBS condition (~11.5%, Figure 6J; 12.5% at 37°C in Figure S5H) was comparable to the case in which periaxonal space width was consistent at the internode and paranode (Figures 6E and 6F).

Finally, we modeled action potential conduction in the fimbria using a parameter set matching the experimental data obtained from NL mice (Figures 6K and 6L; Table S1). The simulated CV was 0.95 m/s (Figure 6L) at 21°C (37°C data in Figure S5L), which is far slower than in CC but is within the range of measured CVs for this region (Corcoba et al., 2015; Jones et al., 1999). Increasing node length by ~30%, to reflect the change produced by RAM learning (Figure 3), increased the simulated CV by 8.9%, while decreasing the periaxonal space width (Figure 5; Table S1) increased CV by 7.3%. Again, implementing all changes measured following learning (Figures 3 and 5; Table S1) had an additive effect, increasing CV by 16.6% (Figure 6L). At 37°C, this is predicted to correspond to a 21.6% increase in CV following learning (Figure S5L). These data suggest that adaptive structural changes at nodes of Ranvier and the periaxonal space act in concert to slow down or speed up action potential conduction along an axon.

iTBS and spatial learning have opposing effects on action potential CV

Because our model predicted that iTBS would slow action potential CV along CC axons, we performed *ex vivo* field potential recordings of compound action potentials (CAPs) in CC of sham and iTBS mice (Figure 7A). The average CV for M axons in CC of sham-stimulated mice was 1.27 ± 0.19 m/s, and this was reduced by ~18% following iTBS (1.04 ± 0.19 m/s) (Figure 7B). The amplitude of the M axon component of the CAP also increased by ~40% following iTBS (Figure 7C) and the half-width decreased by ~9% (Figure 7D), suggesting that a greater number of action potentials arrived simultaneously at the recording electrode. The UM axon component was unaltered by iTBS (Figures 7A–7D). Slowing M axon conduction to this degree did not influence motor coordination, because forelimb swing time, measured during treadmill running (Figure 7E), and the average number of foot-slip errors made crossing a ledged beam (Figure 7F) were unchanged. However, we have previously shown that delivering iTBS to the motor cortex of adult mice can subtly enhance fine-motor-skill learning (Tang et al., 2018), suggesting that modulating CV may facilitate fine-motor-skill acquisition.

To test our *in silico* prediction that RAM learning would increase CV in the fimbria, we performed *ex vivo* CAP recordings at 21°C within the fimbria-fornix pathway of NL and L mice (Figure 7G). Average CV along M axons in the fimbria of NL mice was

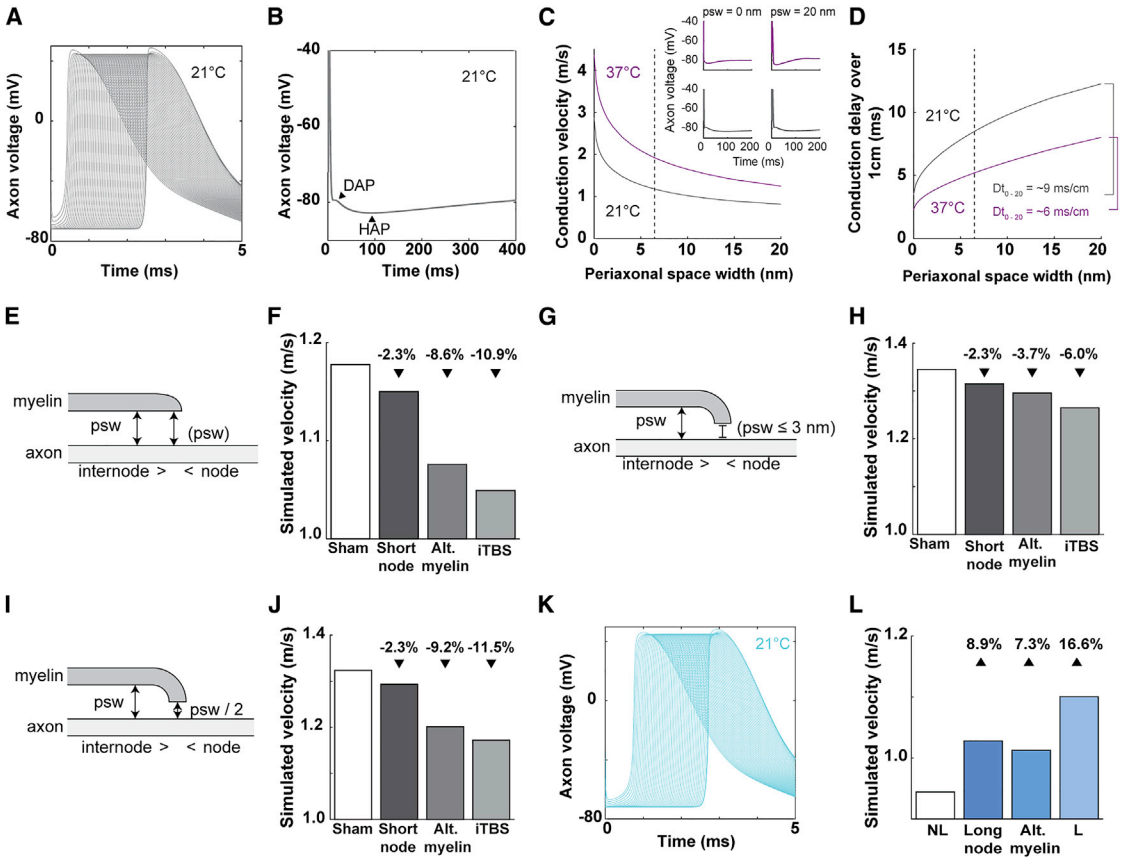

Figure 6. The size of the periaxonal space modulates CV

(A) Action potentials simulated at consecutive callosal nodes at 21°C.

(B) Extended time course of action potentials generated at 21°C, highlighting a slight depolarizing after-potential (DAP) and a hyperpolarizing after-potential (HAP).

(C) Simulated CV of callosal axons relative to periaxonal space width (*psw*) at 37°C (magenta) and 21°C (gray). The dashed line indicates average *psw* following sham stimulation (*psw* = 6.477 nm; 1.18 m/s at 21°C, 1.91 m/s at 37°C), and insets show action potential waveforms at the extremities of the tested range (*psw* = 0 or 20 nm) at 21°C and 37°C.

(D) Conduction delay over 1 cm relative to *psw* at 21°C and 37°C (8.5 ms at 21°C and 5.2 ms at 37°C for *psw* = 6.477 nm).

(E) Schematic showing model parameters in which *psw* at the paranode is uniform to internode *psw*.

(F) Predicted CV of a sham-stimulated axon (white) versus an axon with the node length shortened, the periaxonal space widened, or both (iTBS) using the model depicted in (E).

(G) Schematic showing model parameters in which *psw* at the paranode is set to ≤3 nm.

(H) Predicted CV of a sham-stimulated axon versus an axon with the node length shortened, the periaxonal space widened, or both (iTBS) using the model depicted in (G).

(I) Schematic showing model parameters in which *psw* at the paranode is set to half of the internode *psw*.

(J) Predicted CV of a sham-stimulated axon versus an axon with the node length shortened, the periaxonal space widened, or both (iTBS) using the model depicted in (I).

(K) Action potentials simulated at consecutive nodes within the fimbria at 21°C.

(L) Predicted CV of a NL control axon within the fimbria (white) versus an axon with the nodes lengthened, the *psw* narrowed, or both (L).

See also Figure S5 and Table S1.

0.91 ± 0.3 m/s (Figure 7H) and learning increased CV by ~46% (1.3 ± 0.39 m/s) (Figure 7H). When recordings were made over a larger distance, it was also possible to measure the CV of a distinct population of fast, M axons that conduct at 1.4 ± 0.15 m/s in NL mice (n = 5). Learning again increased CV, this time by ~19% (1.6 ± 0.18 m/s; n = 6; t test, t = 2.594, df = 9, p = 0.02), but it did not alter the peak amplitude (Figure 7I) or half-width (Figure 7J) of the M axon CAP or affect the CV of UM axons (Figures 7H–7J).

Because mice have varying levels of aptitude for RAM learning, we determined how well each mouse performed by subtracting the number of errors made in the first training session from the number of errors made in the last training session. We found that the level of improvement in the RAM task correlated with the M axon CAP CV in the fimbria-fornix pathway (Figure 7K). These data suggest that subtle changes to the ultrastructure of established myelin sheaths may modulate CV to facilitate learning.

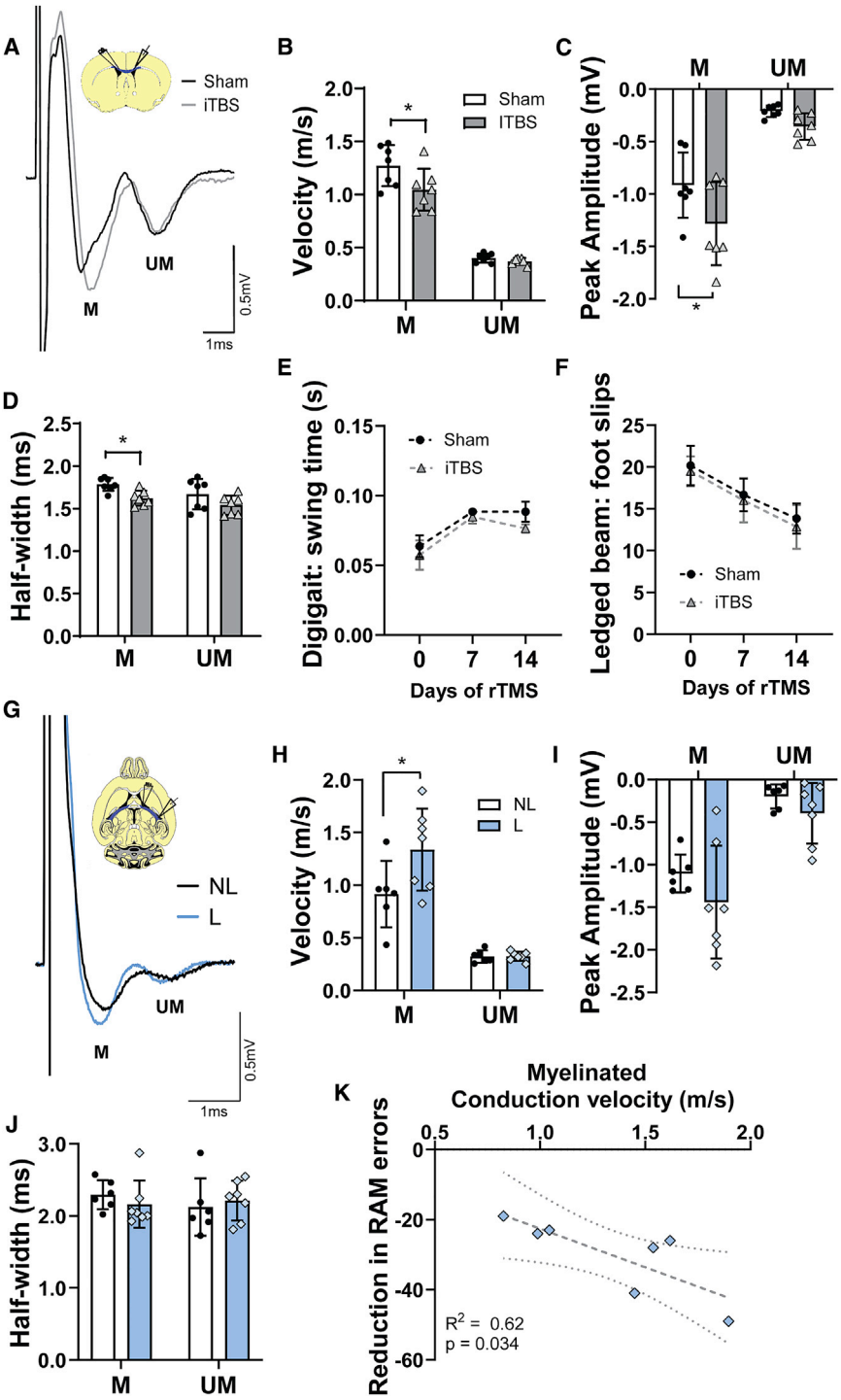

Figure 7. iTBS and spatial learning modulate CV

(A) Compound action potential (CAP) recorded in CC of a sham mouse (black) or iTBS mouse (gray).

(B) CV of myelinated (M) and unmyelinated (UM) axons in sham-stimulated mice (white bars, black circles; n = 7) or iTBS mice (gray bars and triangles; n = 7). 2-way ANOVA: interaction $F(1,24) = 3.37$, $p = 0.078$; axon population $F(1,24) = 211.1$, $p < 0.0001$; treatment $F(1,24) = 5.81$, $p = 0.023$.

(C) Peak amplitude of M and UM axons. 2-way ANOVA: interaction $F(1,24) = 1.25$, $p = 0.27$; axon population $F(1,24) = 68.10$, $p < 0.0001$; treatment $F(1,24) = 6.75$, $p = 0.015$.

(D) Half-width of CAP peak corresponding to M and UM axons. 2-way ANOVA: interaction $F(1,24) = 0.13$, $p = 0.71$; axon population $F(1,24) = 4.63$, $p = 0.04$; treatment $F(1,24) = 10.22$, $p = 0.003$.

(E) Average forelimb swing time during treadmill running at 28 cm/s for sham-stimulated mice (n = 6) and iTBS mice (n = 6) after 0, 7, and 14 days of stimulation. Restricted maximum likelihood (REML) mixed-effect model: interaction $F(2,18) = 0.079$, $p = 0.92$; day $F(1.37,12.36) = 10.62$, $p = 0.004$; treatment $F(1,10) = 1.64$, $p = 0.22$.

(F) Average foot slips made by sham-stimulated and iTBS mice during a ledged-beam task following 0, 7, and 14 days of stimulation. Repeated-measure (RM) 2-way ANOVA: interaction $F(2,20) = 0.006$, $p = 0.99$; day $F(1.91, 19.14) = 7.45$, $p = 0.004$; treatment $F(1,10) = 0.098$, $p = 0.76$.

(G) CAP recorded in the fimbria of mice that underwent NL (black) or L (blue) in the RAM.

(H) CV of M and UM axons in NL mice (white bars, black circles; n = 6) and L mice (blue bars and diamonds; n = 7). 2-way ANOVA: interaction $F(1,22) = 4.35$, $p = 0.048$; axon population $F(1,22) = 63.74$, $p < 0.0001$; training paradigm $F(1,22) = 4.46$, $p = 0.046$.

(I) Peak amplitude of M and UM axons. 2-way ANOVA: interaction $F(1,22) = 0.18$, $p = 0.67$; axon population $F(1,22) = 36.17$, $p < 0.0001$; training paradigm $F(1,22) = 2.72$, $p = 0.11$.

(J) Half-width of M and UM axon CAP peaks. 2-way ANOVA: interaction $F(1,22) = 0.81$, $p = 0.37$; axon population $F(1,22) = 0.24$, $p = 0.62$; training paradigm $F(1,22) = 0.03$, $p = 0.85$.

(K) Reduction in RAM errors made by individual mice (n = 7) from the first training trial to the last training trial versus measured CV of M axons. Simple linear regression: $F(1,5) = 8.33$, $p = 0.032$, $R^2 = 0.6251$, equation $Y = -22.03*X - 0.52$.

Bars show mean ± SD. Line graphs show mean ± SEM (E and F). The linear regression graph (K) shows the line of best fit (dashed line) and 95% confidence bands (dotted lines). *$p < 0.05$ by Bonferroni's post-test.

DISCUSSION

Plasticity of the node of Ranvier

Central myelination is adaptive (for reviews, see Almeida and Lyons, 2017; Bechler et al., 2018; Mount and Monje, 2017; Pepper et al., 2018), and it has been proposed that changing the pattern of myelination within a circuit could profoundly affect neural processing (Pajevic et al., 2014). This area of research has largely focused on the addition of new myelin over time and in response to altered neuronal activity (Cullen et al., 2019; Gibson et al., 2014; Li et al., 2010; McKenzie et al., 2014; Mitew et al., 2018; Sampaio-Baptista et al., 2013; Xiao et al., 2016;

Young et al., 2013), but it is equally important to know whether existing OLs adapt to altered neuronal activity and whether this affects action potential propagation.

Once formed, mature myelinating OLs are long lived (Tripathi et al., 2017), and most internodes they support are stable over time. However, these mature cells retain some capacity to adjust internode length (Auer et al., 2018; Hill et al., 2018). We report that neither iTBS nor spatial learning induces the overt extension or retraction of mature internodes (Figures 1 and 3), which is consistent with sensory enrichment or deprivation failing to alter the existing myelin sheath length within the somatosensory cortex of adult mice (Hughes et al., 2018). However, both iTBS and spatial learning produce a marked change in node length (Figures 2, 3, and 4). Pathological node lengthening (Hinman et al., 2015; Howell et al., 2006; O'Hare Doig et al., 2017; Reimer et al., 2011) is associated with myelin loss (Howell et al., 2006) or paranodal pathology (Huff et al., 2011; Reimer et al., 2011). We found no evidence of myelin pathology following iTBS or learning, and the adaptive changes in node length occurred without a change in paranode length, suggesting that activity-induced nodal plasticity involves a subtle expansion or contraction of the existing myelin internodes without an accompanying change in the number of myelin cytoplasmic loops. Previous studies have suggested that node size could be physiologically modulated as node diameter increases along gerbil globular bushy cell axons, as they approach the calyx of Held (Ford et al., 2015), and node length varies more significantly between CC axons in the rat brain than it does along the length of individual axons (Arancibia-Cárcamo et al., 2017). Although further research is required to uncover the precise mechanics that allow the node of Ranvier to be shortened and lengthened, our data suggest that neuronal activity is a primary driver of nodal plasticity in the adult mouse brain.

Plasticity of the periaxonal space

The direct optogenetic stimulation of layer V pyramidal neurons in the premotor cortex (Gibson et al., 2014), the pharmacogenetic stimulation of layer 2/3 pyramidal neurons in the primary somatosensory cortex (Mitew et al., 2018), and the optogenetic inhibition of parvalbumin$^+$ interneurons in the anterior cingulate cortex (Piscopo et al., 2018) decrease the g-ratio of axons within the underlying CC. iTBS also reduces the g-ratio of CC axons; however, this is not the result of increased myelin thickness or decreased axon diameter but is instead associated with a marked increase in the periaxonal space width (Figure 5). Conversely, spatial learning instead increases the g-ratio of axons within the hippocampal fimbria, but this is also associated with a change (decrease) in the size of the periaxonal space (Figure 5).

The periaxonal space is diminished in mice deficient in myelin-associated glycoprotein (MAG) (Georgiou et al., 2004; Li et al., 1994; Quarles, 2007), a protein expressed specifically in the periaxonal myelin membrane (Pronker et al., 2016), and vacuoles form within this space along optic nerve axons following connexin 32/47 knockout (Menichella et al., 2006). A marked pathological swelling of the periaxonal space has also been observed following acute ischemic white matter injury and demyelination (Aboul-Enein et al., 2003). We did not observe vacuolization, or an uneven separation of the myelin from the axons, suggesting that iTBS- or learning-induced modulation of the periaxonal space is not pathological but rather a physiological adaptation to altered neuronal activity. Although the mechanism underlying this physiological plasticity remains unknown, it may involve MAG or connexin 32/47, be initiated by neurotransmitter receptor activation on the myelin sheath, or result from a change in the movement of ions and metabolites into the periaxonal space in response to neuronal activity (reviewed in Micu et al., 2018).

Nodal and periaxonal plasticities modulate CV

The periaxonal space has been hypothesized to act as a receptacle for calcium, glutamate, and potassium released by the axon during action potential propagation, as well as OL-derived lactate and pyruvate, which are then shuttled through monocarboxylate transporters to provide metabolic support to the axon (reviewed in Micu et al., 2018). It is also an important regulatory element for action potential conduction (Cohen et al., 2020). The periaxonal space is typically narrower at the paranode than under the internode (Nans et al., 2011; Rosenbluth, 1995; Waxman et al., 1995), and the capacity for ultrastructural adaptation of the periaxonal space to influence CV likely depends on its size at both locations. We were unable to measure periaxonal space width at the paranode but incorporated three possible paranodal scenarios into our modeling: (1) the periaxonal space width is uniform under the internode and paranode and changes at both locations, (2) the periaxonal space is narrower under the paranode and does not exceed 3 nm, or (3) the periaxonal space is narrower at the paranode but changes proportionally with the internodal periaxonal space (Figure 6; Figure S5). In all scenarios, adjusting the node length and the internodal periaxonal space width to match the experimental values obtained following iTBS consistently slowed the simulated CVs compared with the sham condition (Figure 6; Figure S5), although the effect was not as strong when the paranodal periaxonal space width remained constant.

When we performed computational modeling to assess the impact that each ultrastructural adaptation measured could have on CV, we found that the iTBS-induced decrease in node length was predicted to slow CV, whereas the learning-induced increase in node length was predicted to increase CV (Figure 6; Figure S5). These data are consistent with a theoretical inverse U relationship between CV and node length in cortical axons, in which nodal sodium channel density has been shown to remain relatively constant across nodes of differing lengths (Arancibia-Cárcamo et al., 2017). In the context of iTBS, our computational modeling suggests that expanding the periaxonal space has a larger effect on action potential slowing than shortening the node length has; however, following spatial learning, increasing node length and decreasing the periaxonal space width sped up action potential conduction to a similar extent. From the data presented, it is not possible to deduce how or even if a change in node length is mechanistically coupled with a change in periaxonal space width. However, our observation that iTBS and RAM learning modified the length of the node of Ranvier and the width of the periaxonal space in a way that ensured a synergistic effect, rather than an opposing effect, on CV makes this an intriguing possibility.

Regulating CV is important for network function

The dynamic modulation of CV could be an adaptive mechanism to ensure the coincident arrival of action potentials at postsynaptic targets. Indeed, when we performed *ex vivo* CAP recordings in CC, we found that iTBS not only slowed CAP CV but also increased the peak amplitude of the CAP response and decreased the half-width, indicating a more synchronized arrival of action potentials at the recording electrode (Figure 7). A larger periaxonal space likely increases the current flowing out of the axon at the internodes and eventually out from underneath the myelin sheath at the node of Ranvier, possibly increasing coupling between neighboring nodes. In other contexts, increased coupling can reduce action potential CV and promote action potential synchronization (Katz and Schmitt, 1940; Schmidt and Knösche, 2019). By contrast, RAM learning increased M axon CAP CV in the fimbria-fornix pathway without altering the peak amplitude or half-width of the CAP response, suggesting that spatial learning acted to increase CV without influencing relative transit times.

At the network level, adjusting action potential arrival times at postsynaptic neurons could influence the probability of postsynaptic firing and determine whether potentiation or depression is induced (Feldman, 2012; Markram et al., 2012). Recent evidence suggests layer V pyramidal and CA3 neurons are highly sensitive to the degree of input synchrony, with asynchronous inputs (even 5 ms apart) producing an action potential of reduced amplitude and reducing the level of spontaneous activity subsequently measured (Zbili et al., 2020). Both theoretical and experimental data have shown that the precise regulation of action potential CV and the firing frequency of neuronal populations is also important for synchronous or time-locked brain wave oscillations (Kato et al., 2020; Noori et al., 2020; Pajevic et al., 2014; Steadman et al., 2020), which are associated with various cognitive functions, including selective attention, information processing, sensory gating of information, learning, memory formation, and consciousness (Ainsworth et al., 2012; Burgess et al., 2007; Buzsaki, 2006; Sirota et al., 2008). Slowing CV by applying iTBS did not lead to overt changes in motor coordination (Figure 7), but it is interesting to speculate that it may facilitate the iTBS-mediated improvement in fine-motor-skill acquisition (Tang et al., 2018). Following RAM learning, we found that the CV of M axons in the fimbria-fornix pathway of individual mice associated with their degree of improvement (learning) (Figure 7), suggesting that adaptive changes in CV may facilitate learning. During spatial learning, oligodendrogenesis increases the coordinated coupling of activity in the hippocampus (CA1) and medial prefrontal cortex to enable memory consolidation (Steadman et al., 2020). Nodal and periaxonal plasticities may be vital homeostatic mechanisms that work in concert with *de novo* myelination to refine action potential CV in response to altered neural circuit activity and in turn influence information coding in the CNS.

STAR★METHODS

Detailed methods are provided in the online version of this paper and include the following:

- KEY RESOURCES TABLE
- RESOURCE AVAILABILITY
  - Lead contact
  - Materials availability
  - Data and code availability
- EXPERIMENTAL MODEL AND SUBJECT DETAILS
- METHOD DETAILS
  - Transgenic lineage tracing and gene deletion
  - Low intensity repetitive transcranial magnetic stimulation
  - DigiGait™ gait analysis
  - Ledge beam task
  - Spatial learning
  - Tissue preparation and immunohistochemistry
  - Confocal microscopy and image quantification
  - Stimulated emission depletion (STED) microscopy
  - Transmission electron microscopy
  - Conduction velocity modeling
  - Compound action potential recordings
- QUANTIFICATION AND STATISTICAL ANALYSIS

SUPPLEMENTAL INFORMATION

Supplemental Information can be found online at https://doi.org/10.1016/j.celrep.2020.108641.

ACKNOWLEDGMENTS

We thank Dr. Rowan Tweedale (the University of Queensland) for constructive feedback on the manuscript. We thank Dr. Lee Cossell and Prof. David Attwell (University College London) for advice on computational modeling and Dr. Carola Thoni and Shane Rix (Lastek: Photonics Technology Solutions, Australia) for assistance with STED imaging. This research was supported by grants from the National Health and Medical Research Council of Australia (NHMRC) (1077792 and 1139041), MS Research Australia (11-014, 16-105, and 17-007), the Australian Research Council (DP180101494), the Medical Research Future Fund (EPCD08), the Swiss National Science Foundation (31003A_170079), and the National MS Society. Fellowships were awarded to C.L.C. (MS Research Australia and the Penn Foundation, 15-054), K.A.P. (NHMRC, 1139180), B.E. (NHMRC, 1032833; Warren endowed professorship in neuroscience research), K.M.Y. (NHMRC, 1045240; MS Research Australia/Macquarie Group Foundation, 17-0223), and J.R. (NHMRC, 1002258; the Perron Institute for Neurological and Translational Science; and MS Western Australia). Scholarships were awarded to L.A. (Australian Postgraduate Award) and to M.T.C. and R.E.P. (Menzies Institute for Medical Research, University of Tasmania).

AUTHOR CONTRIBUTIONS

C.L.C., K.M.Y., R.B.J., R.E.P., K.A.P., J.R., and B.E. developed the project and wrote the manuscript. C.L.C., R.E.P., K.A.P., M.T.C., L.A., V.O., R.B.J., and K.M.Y. carried out the experiments. K.M.Y., J.R., C.L.C., B.E., and R.B.J. obtained the funding. C.L.C., R.E.P., M.T.C., and R.B.J. performed the statistical analyses and generated the figures. K.M.Y., A.D.T., G.R., J.R., and C.L.C. provided supervision.

DECLARATION OF INTERESTS

The authors declare no competing interests.

Received: May 22, 2020
Revised: November 18, 2020
Accepted: December 21, 2020
Published: January 19, 2021

REFERENCES

Aboul-Enein, F., Rauschka, H., Kornek, B., Stadelmann, C., Stefferl, A., Brück, W., Lucchinetti, C., Schmidbauer, M., Jellinger, K., and Lassmann, H. (2003). Preferential loss of myelin-associated glycoprotein reflects hypoxia-like white matter damage in stroke and inflammatory brain diseases. J. Neuropathol. Exp. Neurol. *62*, 25–33.

Ainsworth, M., Lee, S., Cunningham, M.O., Traub, R.D., Kopell, N.J., and Whittington, M.A. (2012). Rates and rhythms: a synergistic view of frequency and temporal coding in neuronal networks. Neuron *75*, 572–583.

Almeida, R.G., and Lyons, D.A. (2017). On myelinated axon plasticity and neuronal circuit formation and function. J. Neurosci. *37*, 10023–10034.

Arancibia-Cárcamo, I.L., Ford, M.C., Cossell, L., Ishida, K., Tohyama, K., and Attwell, D. (2017). Node of Ranvier length as a potential regulator of myelinated axon conduction speed. eLife *6*, e23329.

Auer, F., Vagionitis, S., and Czopka, T. (2018). Evidence for myelin sheath remodeling in the CNS revealed by *in vivo* imaging. Curr. Biol. *28*, 549–559.e3.

Bakiri, Y., Káradóttir, R., Cossell, L., and Attwell, D. (2011). Morphological and electrical properties of oligodendrocytes in the white matter of the corpus callosum and cerebellum. J. Physiol. *589*, 559–573.

Baraban, M., Koudelka, S., and Lyons, D.A. (2018). Ca^{2+} activity signatures of myelin sheath formation and growth *in vivo*. Nat. Neurosci. *21*, 19–23.

Battefeld, A., Popovic, M.A., de Vries, S.I., and Kole, M.H.P. (2019). High-frequency microdomain Ca2+ transients and waves during early myelin internode remodeling. Cell Rep. *26*, 182–191.e5.

Bechler, M.E., Swire, M., and Ffrench-Constant, C. (2018). Intrinsic and adaptive myelination—A sequential mechanism for smart wiring in the brain. Dev. Neurobiol. *78*, 68–79.

Benchenane, K., Peyrache, A., Khamassi, M., Tierney, P.L., Gioanni, Y., Battaglia, F.P., and Wiener, S.I. (2010). Coherent theta oscillations and reorganization of spike timing in the hippocampal-prefrontal network upon learning. Neuron *66*, 921–936.

Bhat, M.A., Rios, J.C., Lu, Y., Garcia-Fresco, G.P., Ching, W., St Martin, M., Li, J., Einheber, S., Chesler, M., Rosenbluth, J., et al. (2001). Axon-glia interactions and the domain organization of myelinated axons requires neurexin IV/Caspr/Paranodin. Neuron *30*, 369–383.

Burgess, N., Barry, C., and O'Keefe, J. (2007). An oscillatory interference model of grid cell firing. Hippocampus *17*, 801–812.

Buzsaki, G. (2006). Rhythms of the brain (Oxford University Press).

Charles, P., Tait, S., Faivre-Sarrailh, C., Barbin, G., Gunn-Moore, F., Denisenko-Nehrbass, N., Guennoc, A.-M., Girault, J.-A., Brophy, P.J., and Lubetzki, C. (2002). Neurofascin is a glial receptor for the paranodin/Caspr-contactin axonal complex at the axoglial junction. Curr. Biol. *12*, 217–220.

Cohen, C.C.H., Popovic, M.A., Klooster, J., Weil, M.-T., Möbius, W., Nave, K.-A., and Kole, M.H.P. (2020). Saltatory conduction along myelinated axons involves a periaxonal nanocircuit. Cell *180*, 311–322.e15.

Corcoba, A., Steullet, P., Duarte, J.M.N., Van de Looij, Y., Monin, A., Cuenod, M., Gruetter, R., and Do, K.Q. (2015). Glutathione deficit affects the integrity and function of the fimbria/fornix and anterior commissure in mice: Relevance for schizophrenia. Int. J. Neuropsychopharmacol. *19*, pyv110.

Crawford, D.K., Mangiardi, M., and Tiwari-Woodruff, S.K. (2009). Assaying the functional effects of demyelination and remyelination: revisiting field potential recordings. J. Neurosci. Methods *182*, 25–33.

Cullen, C.L., Senesi, M., Tang, A.D., Clutterbuck, M.T., Auderset, L., O'Rourke, M.E., Rodger, J., and Young, K.M. (2019). Low-intensity transcranial magnetic stimulation promotes the survival and maturation of newborn oligodendrocytes in the adult mouse brain. Glia *67*, 1462–1477.

Dimou, L., Simon, C., Kirchhoff, F., Takebayashi, H., and Götz, M. (2008). Progeny of Olig2-expressing progenitors in the gray and white matter of the adult mouse cerebral cortex. J. Neurosci. *28*, 10434–10442.

Doerflinger, N.H., Macklin, W.B., and Popko, B. (2003). Inducible site-specific recombination in myelinating cells. Genesis *35*, 63–72.

Dupret, D., O'Neill, J., Pleydell-Bouverie, B., and Csicsvari, J. (2010). The reorganization and reactivation of hippocampal maps predict spatial memory performance. Nat. Neurosci. *13*, 995–1002.

Dupret, D., O'Neill, J., and Csicsvari, J. (2013). Dynamic reconfiguration of hippocampal interneuron circuits during spatial learning. Neuron *78*, 166–180.

Dutta, D.J., Woo, D.H., Lee, P.R., Pajevic, S., Bukalo, O., Huffman, W.C., Wake, H., Basser, P.J., SheikhBahaei, S., Lazarevic, V., et al. (2018). Regulation of myelin structure and conduction velocity by perinodal astrocytes. Proc. Natl. Acad. Sci. USA *115*, 11832–11837.

Emery, B., Agalliu, D., Cahoy, J.D., Watkins, T.A., Dugas, J.C., Mulinyawe, S.B., Ibrahim, A., Ligon, K.L., Rowitch, D.H., and Barres, B.A. (2009). Myelin gene regulatory factor is a critical transcriptional regulator required for CNS myelination. Cell *138*, 172–185.

Etxeberria, A., Hokanson, K.C., Dao, D.Q., Mayoral, S.R., Mei, F., Redmond, S.A., Ullian, E.M., and Chan, J.R. (2016). Dynamic modulation of myelination in response to visual stimuli alters optic nerve conduction velocity. J. Neurosci. *36*, 6937–6948.

Feldman, D.E. (2012). The spike-timing dependence of plasticity. Neuron *75*, 556–571.

Ford, M.C., Alexandrova, O., Cossell, L., Stange-Marten, A., Sinclair, J., Kopp-Scheinpflug, C., Pecka, M., Attwell, D., and Grothe, B. (2015). Tuning of Ranvier node and internode properties in myelinated axons to adjust action potential timing. Nat. Commun. *6*, 8073.

Freeman, S.A., Desmazières, A., Simonnet, J., Gatta, M., Pfeiffer, F., Aigrot, M.S., Rappeneau, Q., Guerreiro, S., Michel, P.P., Yanagawa, Y., et al. (2015). Acceleration of conduction velocity linked to clustering of nodal components precedes myelination. Proc. Natl. Acad. Sci. USA *112*, E321–E328.

Freeman, S.A., Desmazières, A., Fricker, D., Lubetzki, C., and Sol-Foulon, N. (2016). Mechanisms of sodium channel clustering and its influence on axonal impulse conduction. Cell. Mol. Life Sci. *73*, 723–735.

Georgiou, J., Tropak, M.B., and Roder, J.C. (2004). Myelin-associated glycoprotein gene. In Myelin biology and disorders, R.A. Lazzarini, J.W. Griffin, H. Lassman, K.-A. Nave, R. Miller, and B.D. Trapp, eds. (Elsevier), pp. 421–467.

Gibson, E.M., Purger, D., Mount, C.W., Goldstein, A.K., Lin, G.L., Wood, L.S., Inema, I., Miller, S.E., Bieri, G., Zuchero, J.B., et al. (2014). Neuronal activity promotes oligodendrogenesis and adaptive myelination in the mammalian brain. Science *344*, 1252304.

Halter, J.A., and Clark, J.W., Jr. (1993). The influence of nodal constriction on conduction velocity in myelinated nerve fibers. Neuroreport *4*, 89–92.

Hill, R.A., Li, A.M., and Grutzendler, J. (2018). Lifelong cortical myelin plasticity and age-related degeneration in the live mammalian brain. Nat. Neurosci. *21*, 683–695.

Hinman, J.D., Lee, M.D., Tung, S., Vinters, H.V., and Carmichael, S.T. (2015). Molecular disorganization of axons adjacent to human lacunar infarcts. Brain *138*, 736–745.

Hippenmeyer, S., Vrieseling, E., Sigrist, M., Portmann, T., Laengle, C., Ladle, D.R., and Arber, S. (2005). A developmental switch in the response of DRG neurons to ETS transcription factor signaling. PLoS Biol. *3*, e159.

Howell, O.W., Palser, A., Polito, A., Melrose, S., Zonta, B., Scheiermann, C., Vora, A.J., Brophy, P.J., and Reynolds, R. (2006). Disruption of neurofascin localization reveals early changes preceding demyelination and remyelination in multiple sclerosis. Brain *129*, 3173–3185.

Huff, T.B., Shi, Y., Sun, W., Wu, W., Shi, R., and Cheng, J.-X. (2011). Real-time CARS imaging reveals a calpain-dependent pathway for paranodal myelin retraction during high-frequency stimulation. PLoS ONE *6*, e17176.

Hughes, E.G., Orthmann-Murphy, J.L., Langseth, A.J., and Bergles, D.E. (2018). Myelin remodeling through experience-dependent oligodendrogenesis in the adult somatosensory cortex. Nat. Neurosci. *21*, 696–706.

Jakovcevski, I., Filipovic, R., Mo, Z., Rakic, S., and Zecevic, N. (2009). Oligodendrocyte development and the onset of myelination in the human fetal brain. Front. Neuroanat. *3*, 5.

Jeffries, M.A., Urbanek, K., Torres, L., Wendell, S.G., Rubio, M.E., and Fyffe-Maricich, S.L. (2016). Erk1/2 activation in preexisting oligodendrocytes of adult

mice drives new myelin synthesis and enhanced CNS function. J. Neurosci. *36*, 9186–9200.

Jin, J., and Maren, S. (2015). Prefrontal-hippocampal interactions in memory and emotion. Front. Syst. Neurosci. *9*, 170.

Jones, G.A., Norris, S.K., and Henderson, Z. (1999). Conduction velocities and membrane properties of different classes of rat septohippocampal neurons recorded *in vitro*. J. Physiol. *517*, 867–877.

Kang, S.H., Fukaya, M., Yang, J.K., Rothstein, J.D., and Bergles, D.E. (2010). NG2+ CNS glial progenitors remain committed to the oligodendrocyte lineage in postnatal life and following neurodegeneration. Neuron *68*, 668–681.

Kato, D., Wake, H., Lee, P.R., Tachibana, Y., Ono, R., Sugio, S., Tsuji, Y., Tanaka, Y.H., Tanaka, Y.R., Masamizu, Y., et al. (2020). Motor learning requires myelination to reduce asynchrony and spontaneity in neural activity. Glia *68*, 193–210.

Katz, B., and Schmitt, O.H. (1940). Electric interaction between two adjacent nerve fibres. J. Physiol. *97*, 471–488.

Kessaris, N., Fogarty, M., Iannarelli, P., Grist, M., Wegner, M., and Richardson, W.D. (2006). Competing waves of oligodendrocytes in the forebrain and postnatal elimination of an embryonic lineage. Nat. Neurosci. *9*, 173–179.

Klingseisen, A., Ristoiu, A.-M., Kegel, L., Sherman, D.L., Rubio-Brotons, M., Almeida, R.G., Koudelka, S., Benito-Kwiecinski, S.K., Poole, R.J., Brophy, P.J., and Lyons, D.A. (2019). Oligodendrocyte neurofascin independently regulates both myelin targeting and sheath growth in the CNS. Dev. Cell *51*, 730–744.e6.

Koenning, M., Jackson, S., Hay, C.M., Faux, C., Kilpatrick, T.J., Willingham, M., and Emery, B. (2012). Myelin gene regulatory factor is required for maintenance of myelin and mature oligodendrocyte identity in the adult CNS. J. Neurosci. *32*, 12528–12542.

Krasnow, A.M., Ford, M.C., Valdivia, L.E., Wilson, S.W., and Attwell, D. (2018). Regulation of developing myelin sheath elongation by oligodendrocyte calcium transients *in vivo*. Nat. Neurosci. *21*, 24–28.

Li, C., Tropak, M.B., Gerlai, R., Clapoff, S., Abramow-Newerly, W., Trapp, B., Peterson, A., and Roder, J. (1994). Myelination in the absence of myelin-associated glycoprotein. Nature *369*, 747–750.

Li, Q., Brus-Ramer, M., Martin, J.H., and McDonald, J.W. (2010). Electrical stimulation of the medullary pyramid promotes proliferation and differentiation of oligodendrocyte progenitor cells in the corticospinal tract of the adult rat. Neurosci. Lett. *479*, 128–133.

Liu, J., Dietz, K., DeLoyht, J.M., Pedre, X., Kelkar, D., Kaur, J., Vialou, V., Lobo, M.K., Dietz, D.M., Nestler, E.J., et al. (2012). Impaired adult myelination in the prefrontal cortex of socially isolated mice. Nat. Neurosci. *15*, 1621–1623.

Lu, Q.R., Sun, T., Zhu, Z., Ma, N., Garcia, M., Stiles, C.D., and Rowitch, D.H. (2002). Common developmental requirement for Olig function indicates a motor neuron/oligodendrocyte connection. Cell *109*, 75–86.

Makinodan, M., Rosen, K.M., Ito, S., and Corfas, G. (2012). A critical period for social experience-dependent oligodendrocyte maturation and myelination. Science *337*, 1357–1360.

Markram, H., Gerstner, W., and Sjöström, P.J. (2012). Spike-timing-dependent plasticity: a comprehensive overview. Front. Synaptic Neurosci. *4*, 2.

McIntyre, C.C., and Grill, W.M. (2002). Extracellular stimulation of central neurons: influence of stimulus waveform and frequency on neuronal output. J. Neurophysiol. *88*, 1592–1604.

McKenzie, I.A., Ohayon, D., Li, H., de Faria, J.P., Emery, B., Tohyama, K., and Richardson, W.D. (2014). Motor skill learning requires active central myelination. Science *346*, 318–322.

Menichella, D.M., Majdan, M., Awatramani, R., Goodenough, D.A., Sirkowski, E., Scherer, S.S., and Paul, D.L. (2006). Genetic and physiological evidence that oligodendrocyte gap junctions contribute to spatial buffering of potassium released during neuronal activity. J. Neurosci. *26*, 10984–10991.

Micu, I., Plemel, J.R., Caprariello, A.V., Nave, K.-A., and Stys, P.K. (2018). Axo-myelinic neurotransmission: a novel mode of cell signalling in the central nervous system. Nat. Rev. Neurosci. *19*, 49–58.

Mitew, S., Gobius, I., Fenlon, L.R., McDougall, S.J., Hawkes, D., Xing, Y.L., Bujalka, H., Gundlach, A.L., Richards, L.J., Kilpatrick, T.J., et al. (2018). Pharmacogenetic stimulation of neuronal activity increases myelination in an axon-specific manner. Nat. Commun. *9*, 306.

Mount, C.W., and Monje, M. (2017). Wrapped to adapt: Experience-dependent myelination. Neuron *95*, 743–756.

Nans, A., Einheber, S., Salzer, J.L., and Stokes, D.L. (2011). Electron tomography of paranodal septate-like junctions and the associated axonal and glial cytoskeletons in the central nervous system. J. Neurosci. Res. *89*, 310–319.

Negrón-Oyarzo, I., Espinosa, N., Aguilar-Rivera, M., Fuenzalida, M., Aboitiz, F., and Fuentealba, P. (2018). Coordinated prefrontal-hippocampal activity and navigation strategy-related prefrontal firing during spatial memory formation. Proc. Natl. Acad. Sci. USA *115*, 7123–7128.

Noori, R., Park, D., Griffiths, J.D., Bells, S., Frankland, P.W., Mabbott, D., and Lefebvre, J. (2020). Activity-dependent myelination: A glial mechanism of oscillatory self-organization in large-scale brain networks. Proc. Natl. Acad. Sci. USA *117*, 13227–13237.

O'Hare Doig, R.L., Chiha, W., Giacci, M.K., Yates, N.J., Bartlett, C.A., Smith, N.M., Hodgetts, S.I., Harvey, A.R., and Fitzgerald, M. (2017). Specific ion channels contribute to key elements of pathology during secondary degeneration following neurotrauma. BMC Neurosci. *18*, 62.

Osanai, Y., Shimizu, T., Mori, T., Hatanaka, N., Kimori, Y., Kobayashi, K., Koyama, S., Yoshimura, Y., Nambu, A., and Ikenaka, K. (2018). Length of myelin internodes of individual oligodendrocytes is controlled by microenvironment influenced by normal and input-deprived axonal activities in sensory deprived mouse models. Glia *66*, 2514–2525.

Pajevic, S., Basser, P.J., and Fields, R.D. (2014). Role of myelin plasticity in oscillations and synchrony of neuronal activity. Neuroscience *276*, 135–147.

Peles, E., Nativ, M., Lustig, M., Grumet, M., Schilling, J., Martinez, R., Plowman, G.D., and Schlessinger, J. (1997). Identification of a novel contactin-associated transmembrane receptor with multiple domains implicated in protein-protein interactions. EMBO J. *16*, 978–988.

Pepper, R.E., Pitman, K.A., Cullen, C.L., and Young, K.M. (2018). How do cells of the oligodendrocyte lineage affect neuronal circuits to influence motor function, memory and mood? Front. Cell. Neurosci. *12*, 399.

Piscopo, D.M., Weible, A.P., Rothbart, M.K., Posner, M.I., and Niell, C.M. (2018). Changes in white matter in mice resulting from low-frequency brain stimulation. Proc. Natl. Acad. Sci. USA *115*, E6339–E6346.

Pronker, M.F., Lemstra, S., Snijder, J., Heck, A.J.R., Thies-Weesie, D.M.E., Pasterkamp, R.J., and Janssen, B.J.C. (2016). Structural basis of myelin-associated glycoprotein adhesion and signalling. Nat. Commun. *7*, 13584.

Quarles, R.H. (2007). Myelin-associated glycoprotein (MAG): past, present and beyond. J. Neurochem. *100*, 1431–1448.

Reimer, M.M., McQueen, J., Searcy, L., Scullion, G., Zonta, B., Desmazieres, A., Holland, P.R., Smith, J., Gliddon, C., Wood, E.R., et al. (2011). Rapid disruption of axon-glial integrity in response to mild cerebral hypoperfusion. J. Neurosci. *31*, 18185–18194.

Richardson, A.G., McIntyre, C.C., and Grill, W.M. (2000). Modelling the effects of electric fields on nerve fibres: influence of the myelin sheath. Med. Biol. Eng. Comput. *38*, 438–446.

Rivers, L.E., Young, K.M., Rizzi, M., Jamen, F., Psachoulia, K., Wade, A., Kessaris, N., and Richardson, W.D. (2008). PDGFRA/NG2 glia generate myelinating oligodendrocytes and piriform projection neurons in adult mice. Nat. Neurosci. *11*, 1392–1401.

Rosenbluth, J. (1995). Pathology of demyelinated and dysmyelinated axons. In The Axon Structure, Function and Pathophysiology, S.G. Waxman, J.D. Kocsis, and P.K. Stys, eds. (Oxford University Press).

Sampaio-Baptista, C., Khrapitchev, A.A., Foxley, S., Schlagheck, T., Scholz, J., Jbabdi, S., DeLuca, G.C., Miller, K.L., Taylor, A., Thomas, N., et al. (2013). Motor skill learning induces changes in white matter microstructure and myelination. J. Neurosci. *33*, 19499–19503.

Schmidt, H., and Knösche, T.R. (2019). Action potential propagation and synchronisation in myelinated axons. PLoS Comput. Biol. *15*, e1007004.

Schneider, S., Gruart, A., Grade, S., Zhang, Y., Kröger, S., Kirchhoff, F., Eichele, G., Delgado García, J.M., and Dimou, L. (2016). Decrease in newly generated oligodendrocytes leads to motor dysfunctions and changed myelin structures that can be rescued by transplanted cells. Glia *64*, 2201–2218.

Seidl, A.H. (2014). Regulation of conduction time along axons. Neuroscience *276*, 126–134.

Sherman, D.L., Tait, S., Melrose, S., Johnson, R., Zonta, B., Court, F.A., Macklin, W.B., Meek, S., Smith, A.J.H., Cottrell, D.F., and Brophy, P.J. (2005). Neurofascins are required to establish axonal domains for saltatory conduction. Neuron *48*, 737–742.

Simons, M., and Nave, K.A. (2015). Oligodendrocytes: Myelination and axonal support. Cold Spring Harb. Perspect. Biol. *8*, a020479.

Sirota, A., Montgomery, S., Fujisawa, S., Isomura, Y., Zugaro, M., and Buzsáki, G. (2008). Entrainment of neocortical neurons and gamma oscillations by the hippocampal theta rhythm. Neuron *60*, 683–697.

Srinivas, S., Watanabe, T., Lin, C.-S., William, C.M., Tanabe, Y., Jessell, T.M., and Costantini, F. (2001). Cre reporter strains produced by targeted insertion of EYFP and ECFP into the ROSA26 locus. BMC Dev. Biol. *1*, 4.

Steadman, P.E., Xia, F., Ahmed, M., Mocle, A.J., Penning, A.R.A., Geraghty, A.C., Steenland, H.W., Monje, M., Josselyn, S.A., and Frankland, P.W. (2020). Disruption of oligodendrogenesis impairs memory consolidation in adult mice. Neuron *105*, 150–164.e6.

Suzuki, A., Hoshi, T., Ishibashi, T., Hayashi, A., Yamaguchi, Y., and Baba, H. (2004). Paranodal axoglial junction is required for the maintenance of the Nav1.6-type sodium channel in the node of Ranvier in the optic nerves but not in peripheral nerve fibers in the sulfatide-deficient mice. Glia *46*, 274–283.

Tang, A.D., Hong, I., Boddington, L.J., Garrett, A.R., Etherington, S., Reynolds, J.N., and Rodger, J. (2016a). Low-intensity repetitive magnetic stimulation lowers action potential threshold and increases spike firing in layer 5 pyramidal neurons *in vitro*. Neuroscience *335*, 64–71.

Tang, A.D., Lowe, A.S., Garrett, A.R., Woodward, R., Bennett, W., Canty, A.J., Garry, M.I., Hinder, M.R., Summers, J.J., Gersner, R., et al. (2016b). Construction and evaluation of rodent-specific rtms coils. Front. Neural Circuits *10*, 47.

Tang, A.D., Bennett, W., Hadrill, C., Collins, J., Fulopova, B., Wills, K., Bindoff, A., Puri, R., Garry, M.I., Hinder, M.R., et al. (2018). Low intensity repetitive transcranial magnetic stimulation modulates skilled motor learning in adult mice. Sci. Rep. *8*, 4016.

Tripathi, R.B., Jackiewicz, M., McKenzie, I.A., Kougioumtzidou, E., Grist, M., and Richardson, W.D. (2017). Remarkable stability of myelinating oligodendrocytes in mice. Cell Rep. *21*, 316–323.

Waxman, S.G., Kocsis, J.D., and Stys, P.K. (1995). The axon: Structure, function and pathophysiology (Oxford University Press).

Wyss, J.M., Swanson, L.W., and Cowan, W.M. (1980). The organization of the fimbria, dorsal fornix and ventral hippocampal commissure in the rat. Anat. Embryol. (Berl.) *158*, 303–316.

Xiao, L., Ohayon, D., McKenzie, I.A., Sinclair-Wilson, A., Wright, J.L., Fudge, A.D., Emery, B., Li, H., and Richardson, W.D. (2016). Rapid production of new oligodendrocytes is required in the earliest stages of motor-skill learning. Nat. Neurosci. *19*, 1210–1217.

Yeung, M.S., Zdunek, S., Bergmann, O., Bernard, S., Salehpour, M., Alkass, K., Perl, S., Tisdale, J., Possnert, G., Brundin, L., et al. (2014). Dynamics of oligodendrocyte generation and myelination in the human brain. Cell *159*, 766–774.

Young, K.M., Psachoulia, K., Tripathi, R.B., Dunn, S.-J., Cossell, L., Attwell, D., Tohyama, K., and Richardson, W.D. (2013). Oligodendrocyte dynamics in the healthy adult CNS: evidence for myelin remodeling. Neuron *77*, 873–885.

Zbili, M., Rama, S., Yger, P., Inglebert, Y., Boumedine-Guignon, N., Fronzaroli-Moliniere, L., Brette, R., Russier, M., and Debanne, D. (2020). Axonal Na^+ channels detect and transmit levels of input synchrony in local brain circuits. Sci. Adv. *6*, eaay4313.

STAR★METHODS

KEY RESOURCES TABLE

REAGENT or RESOURCE	SOURCE	IDENTIFIER
Antibodies		
Rat (IgG2a) monoclonal (GF090R) anti-GFP	Nacalai Tesque, inc.	Cat# 04404-84; RRID: AB_10013361
Mouse (IgG2b) monoclonal anti-APC (CC-1)	Millipore	Cat# OP80; RRID: AB_2057371
Mouse (IgG1) monoclonal anti-CASPR (Clone K65/35)	UC Davis/NIH NeuroMab Facility	Cat# 75-001; RRID: AB_2083496
Mouse (IgG1) monoclonal anti-NeuN	Millipore	Cat# MAB337; RRID: AB_2298772
Goat (IgG) polyclonal anti-mouse PDGFRα	R & D Systems	Cat# AF1062; RRID: AB_2236897
Rabbit polyclonal anti-OLIG2	Millipore	Cat# AB9610; RRID: AB_570666
Rabbit polyclonal anti-$Na_v1.6$	Alamone labs	Cat# ASC-009; RRID: AB_2040202
Rabbit polyclonal anti-MAP2	Millipore	Cat# AB5622; RRID: AB_91939
Donkey anti-rat Alexa Fluor −488	Thermo Fisher Scientific	Cat# A-21208; RRID: AB_2535794
Donkey anti-mouse Alexa Fluor-568	Thermo Fisher Scientific	Cat# A10037; RRID: AB_2534013
Donkey anti-goat Alexa Fluor-568	Thermo Fisher Scientific	Cat# A-11057; RRID: AB_2534104
Donkey anti-rabbit Alexa Fluor −647	Thermo Fisher Scientific	Cat# A-31573; RRID: AB_2536183
Goat anti-mouse STAR RED	Abberior	Cat# STRED-1001-500UG; RRID: n/a
Goat anti-rabbit STAR Orange	Abberior	Cat# STORANGE-1002-500UG; RRID: n/a
Hoechst 33342	Invitrogen	Cat# H1399; RRID: n/a
Deposited Data		
CV model	This paper	https://github.com/JolivetLab.
Experimental Models: Organisms/Strains		
Mouse / C57BL/6J	The Jackson Laboratories	IMSR Cat# JAX:000664; RRID: IMSR_JAX:000664
Mouse / *Plp-CreER^T*	The Jackson Laboratories	Cat# JAX:005975; RRID: IMSR_JAX:005975
Mouse / *Tau-mGFP*	The Jackson Laboratories	Cat# JAX:021162; RRID: IMSR_JAX:021162
Mouse / *Myrf floxed*	The Jackson Laboratories	Cat# JAX:010607; RRID: IMSR_JAX:010607
Mouse / *Pdgfra-CreER^{TM}*	The Jackson Laboratories	Cat# JAX:018280; RRID: IMSR_JAX:018280
Mouse / *Rosa26-YFP*	The Jackson Laboratories	Cat# JAX:006148; RRID: IMSR_JAX:006148
Oligonucleotides		
Cre 5′ CAGGT CTCAG GAGCT ATGTC CAATT TACTG ACCGTA	Integrated DNA Technologies	n/a
Cre 3′ GGTGT TATAAG CAATCC CCAGAA	Integrated DNA Technologies	n/a
GFP 5′ CCCTG AAGTTC ATCTG CACCAC	Integrated DNA Technologies	n/a
GFP 3′ TTCTC GTTGG GGTCT TTGCTC	Integrated DNA Technologies	n/a
Rosa26 wildtype 5′ AAAGT CGCTC TGAGT TGTTAT	Integrated DNA Technologies	n/a
Rosa26 wildtype 3′ GGAGC GGGAG AAATG GATATG	Integrated DNA Technologies	n/a
Rosa26 YFP 5′ GCGAA GAGTT TGTCC TCAACC	Integrated DNA Technologies	n/a
Myrf 5′ AGGAG TGTTG TGGGA AGTGG	Integrated DNA Technologies	n/a
Myrf 3′ CCCAG GCTGA AGATG GAATA	Integrated DNA Technologies	n/a

(*Continued on next page*)

Continued

REAGENT or RESOURCE	SOURCE	IDENTIFIER
Software and Algorithms		
Fiji (ImageJ)	https://imagej.nih.gov/ij/	RRID: SCR_002285
GraphPad Prism (version 8)	GraphPad Software, Inc.	RRID: SCR_002798
pClamp (version 11)	Molecular Devices	RRID: SCR_011323
MATLAB	Mathworks	RRID: SCR_001622
Volocity 3D Image Analysis Software	Perkin Elmer	RRID: SCR_002668
Other		
Multi-Maze modular system (RAM)	Ugo Basile	Cat# 41500
Kepco Bop 100-4M programmable power supply	TMG test equipment	n/a
BenchLink waveform builder	Agilent Technologies	Part # 33521A
GM08 Gauss Meter, DC and 15Hz - 10kHz	Hirst Magnetic Instruments	n/a
Scientifica SliceScope Pro 1000 electrophysiology rig	Scientifica Ltd.	n/a
Axopatch 200B patch clamp amplifier	Axon Instruments	n/a
Iso-Stim 01D stimulus isolator	NPI Electronic	n/a
DigiGait™ gait analysis system	Mouse Specifics, Inc.	n/a

RESOURCE AVAILABILITY

Lead contact

Further information and requests for resources and reagents should be directed to and will be fulfilled by the lead contact, Kaylene Young (Kaylene.Young@utas.edu.au).

Materials availability

This study did not generate new unique reagents.

Data and code availability

All data generated and analyzed for this study is included in the manuscript. Data and code for computational modeling are available from GitHub (https://github.com/JolivetLab).

EXPERIMENTAL MODEL AND SUBJECT DETAILS

All animal experiments were approved by the University of Tasmania Animal Ethics Committee and carried out in accordance with the Australian code of practice for the care and use of animals for scientific purposes. All wild-type and transgenic mice were maintained on a C57BL/6J background. Heterozygous *Plp-CreER* transgenic mice (Doerflinger et al., 2003) were crossed with heterozygous *Tau-lox-STOP-lox-mGFP-IRES-NLS-LacZ-pA* (*Tau-mGFP*) Cre-sensitive reporter mice (Hippenmeyer et al., 2005) to generate double heterozygous offspring for the fluorescent labeling and tracing of OLs. Heterozygous *Pdgfra-CreER*^{TM} transgenic mice (Kang et al., 2010) were crossed with homozygous *Rosa26-YFP Cre*-sensitive reporter mice (Srinivas et al., 2001) to generate double heterozygous offspring for the fluorescent labeling and tracing of OPCs and the newborn cells they produce. Homozygous *Myrf* loxP-flanked exon 8 mice (*Myrf*$^{fl/fl}$) (Emery et al., 2009) were crossed with heterozygous *Pdgfra-CreER*^{TM} transgenic mice (Kang et al., 2010) or homozygous *Rosa26-YFP Cre*-sensitive reporter mice (Srinivas et al., 2001) to produce *Pdgfra-CreER*^{TM}*:: Myrf*$^{fl/fl}$ and *Myrf*$^{fl/fl}$*:: Rosa26-YFP* offspring, respectively. These offspring were then intercrossed to generate *Pdgfra-CreER*^{TM}*:: Rosa26-YFP:: Myrf*$^{fl/fl}$ (Myrf$^{fl/fl}$) and *Rosa26-YFP:: Myrf*$^{fl/fl}$ (control) mice for experiments. Male and female mice were housed in same sex groups (2-4 per cage), in individually ventilated cages (Optimice®) on a 12 h light cycle (twilight phase starts 06:30, full lights on 07:00) at 21 ± 2°C with *ad libitum* access to standard rodent chow (Barrastoc rat and mouse pellets) and water. Experimental mice (P60-P90) weighed 18-35 g at the start of experiments and were randomly assigned to each treatment, but care was taken to ensure littermates were represented across treatment groups.

METHOD DETAILS

Transgenic lineage tracing and gene deletion

Cre, *Rosa26-YFP* and *Tau-mGFP* transgenes were detected by PCR as described by Cullen et al. (2019), and the *Myrf*^{floxed} gene was detected as described by Emery et al. (2009). In brief, genomic DNA (gDNA) was extracted from ear biopsies by ethanol precipitation and PCR was performed using 50-100ng of gDNA with the following primer combinations: Cre 5′ CAGGT CTCAG GAGCT ATGTC

CAATT TACTG ACCGTA and Cre 3′ GGTGT TATAAG CAATCC CCAGAA; GFP 5′ CCCTG AAGTTC ATCTG CACCAC and GFP 3′ TTCTC GTTGG GGTCT TTGCTC; Rosa26 wild-type 5′ AAAGT CGCTC TGAGT TGTTAT, Rosa26 wild-type 3′ GGAGC GGGAG AAATG GATATG and Rosa26 YFP 5′ GCGAA GAGTT TGTCC TCAACC; Myrf 5′ AGGAG TGTTG TGGGA AGTGG and Myrf 3′ CCCAG GCTGA AGATG GAATA.

To activate Cre-recombinase in OPCs and induce targeted DNA recombination, Tamoxifen was dissolved in corn oil (40mg/ml) by sonication at 21°C for 2 h and administered to adult mice (P60-P83) by oral gavage at a dose of 300mg tamoxifen/kg body weight daily for four consecutive days. *Plp-CreER:: Tau-mGFP* mice were given a single dose of 50mg/kg, 100mg/kg or 300mg/kg body weight to enable clear visualization of individual $mGFP^{+}$ internodes (Figure S1).

Low intensity repetitive transcranial magnetic stimulation

Low intensity repetitive transcranial magnetic stimulation (Li-rTMS) was delivered as per Cullen et al. (2019). Briefly, 600 pulses of intermittent theta burst stimulation (iTBS; 192 s) was delivered using a custom made 120mT circular coil designed for rodent stimulation (8mm outer diameter, iron core) (Tang et al., 2016a, 2016b). Stimulation parameters were controlled by a waveform generator (Agilent Technologies) connected to a bipolar voltage programmable power supply (KEPCO BOP 100-4M, TMG test equipment). Experiments were conducted at 100% maximum power output (100V) using custom monophasic waveforms (400μs rise time; Agilent Benchlink Waveform Builder). Mice were restrained using plastic body-contour shape restraint cones (0.5mm thick; Able Scientific). The coil was manually held over the midline of the head with the back of the coil positioned in line with the front of the ears (~Bregma −3.0). Sham mice were positioned under the coil for 192 s (as per iTBS), but no current was passed through the coil. Stimulation was carried out once daily, at the same time, for 7, 14 or 28 consecutive days. Li-rTMS did not elicit observable behavioral changes in the mice during or immediately after stimulation.

DigiGait™ gait analysis

Gait analysis was performed using the DigiGait™ treadmill imaging system (Mouse Specifics, Inc). Prior to, and again after 7 and 14 days of iTBS or sham stimulation, mice were habituated to the treadmill enclosure for 5 min before the treadmill was turned on and the speed of the transparent belt increased from 10cm/s to 28cm/s over 2 min. Short ~10 s videos were recorded from underneath the mice as they ran at a belt speed of 28cm/s. The 10 s videos were cut to a length of ~3-4 s in which mice were running straight without obvious acceleration or deceleration, by an experimenter blind to treatment group. The short video clips were analyzed using the semi-automated DigiGait™ analysis software. Each digital analysis output was then cross checked for processing errors (e.g., a forepaw mistakenly labeled as a hind paw) and corrected, if required, before data were exported for statistical analysis.

Ledge beam task

Motor balance and coordination was assessed using the ledged beam task prior to, and after 7 and 14 days of iTBS or sham-stimulation. Mice were placed at the lower (wider) end of a plexiglass beam that tapered from 3.5cm to 0.5cm over a length of 50 cm and was placed at an incline of 30 degrees. A peripheral ledge (0.5cm wide) ran along each side of the beam, 1cm below the top. After an initial training session, mice were video recorded as they ran up the beam and into their home cage, located at the narrow end. These videos were manually scored for foot slips by an experienced experimenter blind to the treatment groups. A foot slip was scored when a mouse placed any paw on the peripheral ledge instead of the central beam.

Spatial learning

To induce spatial learning, adult (P60) male and female *Plp-CreER:: Tau-mGFP* or littermate control mice were administered a single dose of tamoxifen (50mg/kg), then handled daily for two weeks before being trained in an 8-arm radial arm maze (RAM) task (Figure S3) over 14 days. 5 days prior to RAM training, non-learning and learning mice had their access to normal mouse chow restricted to 6h per day but were given food rewards (Froot Loops® pieces) in their home cage. This food restriction protocol ensured that mice were maintained at ~90% of their free feeding body weight and were motivated to seek out and consume the food rewards when available.

The RAM was carried out using the multi-maze system for mice (Ugo-Basile) in a radial 8-arm configuration with spatial cues placed on each of the surrounding walls, ~30cm above the maze. RAM training consisted of two phases - a familiarization phase (days 1-3) and a learning phase (days 4-14) (Figure S3), and each mouse underwent 3 trials per day, with 60 min between each trial. During the familiarization phase, all arms of the RAM were closed off and an individual mouse was placed in the octagonal center of the maze with a single Froot Loop® (cut into 8 approximately equal sized pieces) for 10 min. No-learning control mice were returned to the familiarization phase conditions for the 14 days of the task, to ensure that they were subjected to the same environment and an equivalent level of handling and that they also received Froot Loops®, but did not learn the RAM task (Figure S3A). Learning mice proceeded to undertake a learning phase, in which the 8 pieces of Froot Loop® were distributed, so that one piece was placed at the end of each arm of the RAM. An individual mouse was placed in the center of the maze and could explore the maze for 10 min (Figure S3B). Over the next 11 days, the mice learned that each arm contained a single food reward and that repeat entries would not result in another reward. Therefore, repeated entries into an arm in which the food reward had already been consumed was counted as an error, and the average number of errors made per trial was quantified as a measure of learning (Figure S3C). 24 h after the final trial, mice were either perfusion fixed and their brains collected and prepared for either fluorescent or transmission electron microscopy, or were used to generate acute brain slices for compound action potential recordings.

Tissue preparation and immunohistochemistry

Mice were perfusion-fixed with 4% paraformaldehyde (PFA; Sigma) (w/v) in phosphate buffered saline (PBS). Brains were cut into 2mm-thick coronal slices using a 1mm brain matrix (Kent Scientific) before being post-fixed in 4% PFA at 21°C for 90 min. Tissue was cryoprotected overnight in 20% (w/v) sucrose (Sigma) in PBS and snap frozen in OCT (ThermoFisher) for storage at −80°C. 30μm coronal brain cryosections, containing the primary motor cortex and underlying corpus callosum (~Bregma +0.5) or the dorsal region of the fimbria (~Bregma −1.5), were collected and processed as floating sections (Cullen et al., 2019). Primary and secondary antibodies were diluted in PBS blocking solution [0.1% (v/v) Triton X-100 and 10% fetal calf serum in PBS] and applied to sections overnight at 4°C, unless staining involved the use of mouse anti-CC1 (1:100 Calbiochem), in which case antibodies were diluted in Tris buffered saline (TBS) blocking solution [0.1% (v/v) Triton X-100 and 10% fetal calf serum in TBS]. Primary antibodies included goat anti-PDGFRα (1:200; R&D Systems), rabbit anti-OLIG2 (1:400 Millipore), rat anti-GFP (1:2000; Nacalai Tesque), rabbit anti-$NaV_{1.6}$ (1:500 Alomone Labs), mouse anti-CASPR (Clone K65/35; 1:200 NeuroMab), mouse anti-NeuN (1:200 Millipore) and rabbit anti-MAP2 (1:1000 Millipore). Secondary antibodies, which were conjugated to AlexaFluor −488, −568 or −647 (Invitrogen) were donkey anti-goat (1:1000), donkey anti-rabbit (1:1000), donkey anti-mouse (1:1000), and donkey anti-rat (1:500). Nuclei were labeled using Hoechst 33342 (1:1000; Invitrogen).

Confocal microscopy and image quantification

Confocal images were collected using an UltraView Nikon Ti Microscope with Volocity Software (Perkin Elmer). High-magnification images (z-spacing of 0.5-2μm) were collected using standard excitation and emission filters for DAPI, FITC (AlexaFluor-488), TRITC (AlexaFluor-568) and CY5 (AlexaFluor-647), then stitched together to make a composite image of a defined region of interest. To quantify internode number and length for OLs within the primary motor cortex (M1), high-magnification images (40x objective) were collected through individual mGFP-labeled cortical OLs (0.5μm z-steps) that had a visible cell body. To quantify internodes in the corpus callosum (CC) and hippocampal fimbria, high-magnification images (60x objective) were collected (0.5μm z-steps) and used to identify individual mGFP-labeled internodes that were flanked by $CASPR^+$ paranodes. To measure node of Ranvier ($Na_v1.6$) and paranode (CASPR) length, high-magnification (100x) single z-plane confocal images were collected from M1, the CC and the fimbria. Node and paranode lengths were only measured when a node and its flanking paranodes were intact within the single z-plane. To measure neuronal soma size within M1, high-magnification (40x objective) confocal images (0.5μm z-steps) were collected from 5 fields of view and used to identify and measure $NeuN^+$ soma that were enveloped by a clear $MAP2^+$ ring. For quantification of cell number, low-magnification (20x objective) confocal z stacks (2 μm spacing) were collected through M1, CC or the hippocampal fimbria and stitched together to make a composite image of a defined region of interest. All image analysis was carried out using ImageJ (NIH) by a researcher blind to experimental treatment.

Stimulated emission depletion (STED) microscopy

30μm coronal cryosections containing the CC (~Bregma +0.5) were collected and prepared as floating sections. Rabbit anti-$Na_v1.6$ (1:500 Alomone Labs) and mouse anti-CASPR (Clone K65/35; 1:200 NeuroMab) primary antibodies were diluted in PBS blocking solution [0.1% (v/v) Triton X-100 and 10% fetal calf serum in PBS] and applied to sections overnight at 4°C. The sections were washed in PBS (3 × 10 min) before overnight application (4°C) of goat anti-mouse STAR Red (1:500, Abberior) and goat anti-rabbit STAR Orange (1:500, Abberior) secondary antibodies. The sections were mounted in antifade liquid mounting media (Abberior) and covered in a 170 μm thick glass coverslip (ProSciTech, cat # EMS72291-06).

STED imaging was performed using a two-color Abberior STEDYCON system (Abberior Instruments GmbH) attached to a Nikon NiE confocal microscope equipped with 405nm, 488 nm, 561 nm, and 640 nm pulsed excitation lasers, a pulsed 775 nm STED laser and a 100x oil immersion objective lens (N.A 1.4). Images were acquired using Abberior STEDYCON smart control software. For all images the pixel size and dwell time were kept consistent at 20nm and 10μs, respectively. 561nm and 640nm excitation lasers were set to 10% power but STED laser power was optimally set to 100% (STAR orange, 561nm) or 56.2% (STAR red, 640nm). Single z-plane STED images were collected from the CC to enable the precise, high-resolution visualization of nodes of Ranvier ($Na_v1.6$) and their abutting paranodes (CASPR).

Transmission electron microscopy

Following 14 days of iTBS, sham stimulation or RAM training, P105 or P89 mice were perfused with Karnovsky's fixative (2.5% glutaraldehyde, 2% PFA, 0.25mM $CaCl_2$, 0.5mM $MgCl_2$ in 0.1M sodium cacodylate buffer). Brains were cut into 1mm-thick coronal slices using a 1mm brain matrix (Kent Scientific) and post-fixed in Karnovsky's fixative for 2h at 21°C. The tissue blocks were rinsed and stored in 0.1M sodium cacodylate buffer overnight. The medial part of the CC (~Bregma +0.5 to −0.5) or hippocampal fimbria (~Bregma −1.0 to −2.0) was dissected and incubated in 1% osmium tetroxide / 1.5% potassium ferricyanide [OsO_4 / $K_3Fe(III)(CN)_6$] in 0.1M sodium cacodylate buffer in the dark for 2h at 4°C, before being dehydrated in ethanol and propylene oxide, and embedded in Epon812 resin. Ultrathin 70nm sections were cut using a Leica Ultra-cut UCT7 and stained with uranyl acetate and lead citrate. High resolution electron microscopy imaging was done at 80kV on a JEOL 1400-Flash (CC) or a Hitachi HT7700 (fimbria) transmission electron microscope. Sectioning, imaging, and image analysis was carried out by an experimenter blind to the treatment group.

Image analysis was carried out using ImageJ (NIH). The proportion of myelinated axons and the g-ratio of myelinated axons [axon diameter / (axon + myelin diameter)] were measured from at least 100 axons from 5 images per animal. The number of myelin wraps

was quantified by counting major dense lines for a minimum of 15 transected axons per mouse, from n = 3 mice per treatment group. The cross-sectional area of the adaxonal inner tongue membrane was quantified by tracing the outer edge of the inner tongue using the polygon selection tool in ImageJ. The average thickness of myelin wraps per axon, and the width of the periaxonal space were measured from ultra-high-magnification (×120-200k) images of axons ensheathed by compact myelin a minimum of five wraps thick (≥10 transected axons per mouse, from n = 3 mice per treatment group). To ensure unbiased axon sampling and measurements of the periaxonal space width, high-magnification images were collected by an experimenter blind to treatment condition. These coded images were then analyzed by a second experimenter and decoded after quantification was complete.

Conduction velocity modeling

In order to evaluate the effect on action potential propagation of experimentally observed changes in node length and myelin structure, i.e., periaxonal space width + associated change in g-ratio, [data derived from the population mean from n = 3 animals for iTBS experiments (Figures 1, 2, and 5; Figure S2) and n = 3-4 animals for RAM experiments (Figures 3 and 5; Figure S3)], we further adapted the mathematical model of action potential propagation in myelinated axons proposed by Richardson and colleagues (model 'C', their figure 1; Bakiri et al., 2011; Richardson et al., 2000). A recent MATLAB (The MathWorks) implementation of that model by Cossell and colleagues can be downloaded from GitHub (https://github.com/AttwellLab/MyelinatedAxonModel) (Arancibia-Cárcamo et al., 2017; Bakiri et al., 2011; Ford et al., 2015; Young et al., 2013). That package was downloaded in June 2018 and run on MATLAB R2016b.

The mathematical description of ion channels at nodes of Ranvier follows the Hodgkin-Huxley formalism. Briefly, nodes express three types of ion channels, a fast sodium channel i_{Na}^{fast} responsible for the initiation of action potentials, a persistent sodium channel $i_{Na}^{persistent}$, and a slow potassium channel i_{K}^{slow} responsible for the termination of action potentials. The kinetics of the three currents is derived from McIntyre and Grill (2002). Briefly, i_{Na}^{fast} is written:

$$i_{Na}^{fast} = g_{Naf}\, m^3\, h\, (V - E_{Na}) \tag{1}$$

with g_{Naf} the current conductance, V the membrane voltage at the node, $E_{Na} = 60$mV the reversal potential for sodium ions, and m and h some gating variables. Following the Hodgkin-Huxley formalism, each gating variable x in the model follows the generic equation:

$$\frac{dx}{dt} = \alpha_x(1 - x) - \beta_x x \tag{2}$$

with α and β some functions of V. For i_{Na}^{fast}, α and β are given by:

$$\alpha_m = 6.57\frac{V + 20.4}{1 - e^{-\frac{V+20.4}{10.3}}} \tag{3}$$

$$\beta_m = -0.304\frac{V + 25.7}{1 - e^{\frac{V+25.7}{9.16}}} \tag{4}$$

$$\alpha_h = -0.34\frac{V + 114}{1 - e^{\frac{V+114}{11}}} \tag{5}$$

$$\beta_h = \frac{12.6}{1 + e^{-\frac{V+31.8}{13.4}}}. \tag{6}$$

The persistent sodium current $i_{Na}^{persistent}$ is given by:

$$i_{Na}^{persistent} = g_{Nap}\, p^3\, (V - E_{Na}) \tag{7}$$

with:

$$\alpha_p = 0.0353\frac{V + 27}{1 - e^{-\frac{V+27}{10.2}}} \tag{8}$$

$$\beta_p = -0.000883\frac{V + 34}{1 - e^{(V+34)/10)}}. \tag{9}$$

The slow potassium current i_{K}^{slow} is given by:

$$i_{K}^{slow} = g_K\, s\, (V - E_K) \tag{10}$$

with $E_K = -90$mV the reversal potential for potassium ions and:

$$\alpha_s = \frac{0.3}{1 + e^{-\frac{V+53}{5}}} \tag{11}$$

$$\beta_s = \frac{0.03}{1 + e^{-(V+90)}}. \tag{12}$$

Finally, all membranes contain a leak current given by:

$$i_L = g_L\,(V - E_L). \tag{13}$$

The Q10 for gates *m*, *h*, *p,* and *s* are 2.2, 2.9, 2.2 and 3.0 respectively, described at 36°C [note that this has the effect of slowing down the kinetics of gates *m*, *h,* and *p* with respect to McIntyre and Grill (2002)]. All the other parameters of the model are given in Table S1. The same framework was used to simulate both *corpus callosum* and *fimbria* axons but with different parameter sets (see Table S1). All numerical values were set to the average values measured for the sham or no-learning experimental groups, with the exception of parameters that were significantly different following iTBS or learning – in these cases the sham, iTBS, no-learning or learning values were directly entered into the model (see Table S1). Parameters that were not obtained from our experimental data were adapted from Arancibia-Cárcamo et al. (2017). Myelin thickness was automatically calculated using:

$$\text{Myelin thickness} = (d\,/\,g - d - 2\,psw)/2 \tag{14}$$

with *d* the axon diameter, *g* the g-ratio and *psw* the periaxonal space width. Myelin lamella periodicity was taken as myelin thickness divided by 6.5 so that the number of wraps is 7 in all conditions as observed experimentally (see Figure 5), assuming that the extracellular space between myelin lamellae comprises part of the periodicity, and to account for the fact that there is no extracellular space contributing to the total width of the myelin on the most external lamella. Note that as the number of wraps does not change between any of the conditions, changes in myelin thickness reflect the addition – or subtraction – of cytoplasmic space between lipid bilayers. Adding or removing cytoplasmic space filled with intracellular solution between lipid bilayers does not significantly affect the resistance or capacitance across myelin wraps, and thus does not affect CV (see Figure S5O).

Unless stated otherwise, simulations were run using a time step of 0.1μs and 51 nodes. Internode segments were chosen to be < 1μm (0.98μm; n = 52 segments per internode) and we verified that this was sufficient to reach convergence for the CV over the whole range of simulated axons (Figure S5). Action potentials were triggered by a square pulse of 0.5nA lasting 10μs. Ion channels at juxtaparanodes were not modeled, as is common in the field. When altering the length of the node of Ranvier (see below), the density of ion channels at the node was taken to be constant (see Arancibia-Cárcamo et al., 2017, for a systematic discussion of how this affects action potential CV).

To evaluate individually the effect of a node length reduction or a change in the myelin sheath (i.e., increase in periaxonal space width + accompanying decrease in g-ratio) on CV, we initially ran four sets of simulations. First, we used a parameter set matching the observations obtained in the sham condition (column 'Sham' in Table S1). We then ran the same simulations after reducing node lengths ('Short nodes'). Third, we ran simulations modifying the myelin sheath but keeping node length as per the sham condition ('Alt. myelin'). Finally, we ran a simulation with a fourth set of parameters implementing both of the experimental changes observed following iTBS, i.e., a reduction in node length and altered myelin sheath (change in periaxonal space + corresponding change in g-ratio). Simulations were run at 21°C and at 37°C (Figure 6; Figure S5). We additionally investigated three different scenarios for conduction at the paranode. The periaxonal space width at the paranode was taken to be either [i] equal to the periaxonal space width in the internode; [ii] equal to the periaxonal space width under the internode if that is less than 3nm, but to be at most 3nm otherwise; or [iii] equal to half the periaxonal space width in the internode (Figure 6; Figure S5). Unless otherwise specified, scenario [i] is in use. Each paranode was taken to be 2 segments long (1.96μm long).

To evaluate the functional consequence of myelin alterations, we additionally ran a set of simulations varying the periaxonal space width from 0 to 20nm at both 21°C and 37°C (Figure 6). These simulations show that at 37°C, the periaxonal space can shift action potential CV between 4.36 m/s (psw = 0nm) and 1.25 m/s (psw = 20nm; Figure 6). These numbers illustrate how potent and elegant this mechanism is, as it can speed up or slow down action potential conduction by a factor of 3.5 by making minor adjustments to the structure of myelinated axons. The functional consequences of this change to propagation speed at 37°C is to alter the arrival time of action potentials by 6ms over a distance of 1cm (Figure 6), enough to alter learning via spike-timing dependent plasticity for instance.

Finally, Cohen et al. (2020) recently reported different values for the axonal and periaxonal space resistivities. In particular, they reported that the axonal resistivity is about three times larger than the periaxonal space resistivity. In order to evaluate how this would impact our results, we simulated conduction by cortical axons (see Figure 6; Figure S5) using the resistivity values reported by Cohen et al. (2020) (axonal resistivity = 1.5 Ω·m; periaxonal space resistivity = 0.54 Ω·m), and adapting the conductance of some ionic channels at nodes of Ranvier to match action potential conduction velocities to those reported in Figure 6 and S5 (Figure S6; g_{Naf} = 550 mS/mm^2, g_K = 24 mS/mm^2). With these new parameters, we observe a slight reduction of the effects reported in Figures 6 and S5, but still find that adjusting the periaxonal space width effectively modulates action potential CV (Figure S6).

Compound action potential recordings

Compound action potential (CAP) recording and conduction-velocity measurement procedures were adapted from Crawford et al. (2009). Briefly, the day after LI-rTMS or RAM training was complete, mice were killed by cervical dislocation and their brains rapidly dissected into ice-cold sucrose solution containing: 75 mM sucrose, 87 mM NaCl, 2.5 mM KCl, 1.25 mM NaH_2PO_4, 25 mM $NaHCO_3$, 7 mM $MgCl_2$, and 0.95 mM $CaCl_2$. For recordings from the CC, 400 μm live coronal brain vibratome (Leica VT1200s) slices were generated spanning Bregma +0.8 and −0.2. For recordings from the fimbria-fornix pathway, 400 μm live horizontal brain vibratome sections were generated at Bregma −2.36 and −2.56. All slices were incubated at ~32°C for 45 min in artificial cerebral spinal fluid (ACSF) containing 119 mM NaCl, 1.6 mM KCl, 1 mM NaH_2PO4, 26.2 mM $NaHCO_3$, 1.4 mM $MgCl_2$, 2.4 mM $CaCl_2$ and 11 mM glucose (300 ± 5 mOsm / kg), before being transferred to ~21°C ACSF saturated with 95% O_2/5% CO_2.

CAPs were evoked by constant current, stimulus-isolated, square wave pulses (200 ms duration, delivered at 0.2 Hz), using a tungsten bipolar matrix stimulating electrode (FHC; MX21AEW), and detected using glass recording electrodes (1-3 MΩ) filled with 3M NaCl. To quantify CAP amplitude, the asymptotic maximum for the short-latency negative peak (myelinated peak, M; Figure 7) was first determined by placing the stimulating and recording electrodes 1mm apart and varying the intensity of stimulus pulses (0.3–4.0 mA) using an external stimulus isolator (ISO-STIM 1D) before recording at 80% maximum stimulation. To enhance the signal-to-noise ratio, all quantitative electrophysiological analyses were conducted on waveforms that were the average of eight successive sweeps, amplified, and filtered (10 kHz low pass bessel) using an Axopatch 200B amplifier (Molecular Devices), digitized at 100 kHz and stored on disk for offline analysis.

The CV of myelinated (M) and unmyelinated (UM) axons was estimated by changing the distance between the stimulating and recording electrodes from 1 to 3 mm for the CC and 0.5 to 2.5 mm for the fimbria, while holding the stimulus intensity constant (80% maximum). The peak latency of the M and UM axons was measured at each point and graphed relative to the distance separating the electrodes. A linear regression analysis was then performed to yield a slope that is the inverse of the velocity for each brain slice. The average velocity for both CAP components (M, UM) was then determined for each animal and this value was used for statistical comparison. Within the fimbria-fornix pathway, when the stimulating and recording electrodes were placed far enough apart (~2mm) a response peak from a third population of fast, myelinated axons became apparent in recordings from 11/13 mice (n = 5 NL; n = 6 L mice). As this response peak was not present at all distances, the CV for this population of fast myelinated axons was estimated as a construct of distance/time [distance between electrodes / time to response peak].

QUANTIFICATION AND STATISTICAL ANALYSIS

The number of mice analyzed in each group (*n*) or the number of cells, axons, nodes or internodes is indicated in the corresponding figure legends. Data distributions are presented as cumulative distribution plots and as violin plots with the median and interquartile range indicated. Data averaged per animal are presented as mean ± SD with all data points shown. All statistical analyses were performed using Prism 8 (GraphPad Software). Data comparing two groups at a single time point were analyzed using a parametric two-tailed t test (n = mouse) or a non-parametric Mann-Whitney U test (MWU; n = node, paranode, internode or axon). Cumulative distribution data were analyzed using a Kolmogorov–Smirnov (KS) test. Cell counts for lineage tracing, and compound action potential data were analyzed using a 2-way ANOVA with Bonferroni post-test. Learning in the RAM was analyzed using a repeated-measures (RM) one-way ANOVA with a Geisser-Greenhouse correction to ensure equal variability and sphericity was not assumed, followed by a Bonferroni post-test. Foot slips in the ledged beam task were analyzed using a RM 2-way ANOVA with a Geisser-Greenhouse correction followed by a Bonferroni post-test. Gait parameters from the DigiGait treadmill were analyzed using a restricted maximum likelihood (REML) mixed effects model with a Geisser-Greenhouse correction followed by a Bonferroni post-test, as gait parameters could not be obtained for two animals (n = 2 iTBS mice) at the 7 day time point. ANOVA main effects are given in the corresponding figure legends. The relationship between CV and error reduction in the RAM was analyzed using a simple linear regression model and all details are reported in the corresponding figure legend.

Cell Reports, Volume *34*

Supplemental Information

Periaxonal and nodal plasticities modulate action potential conduction in the adult mouse brain

Carlie L. Cullen, Renee E. Pepper, Mackenzie T. Clutterbuck, Kimberley A. Pitman, Viola Oorschot, Loic Auderset, Alexander D. Tang, Georg Ramm, Ben Emery, Jennifer Rodger, Renaud B. Jolivet, and Kaylene M. Young

Supplemental material:

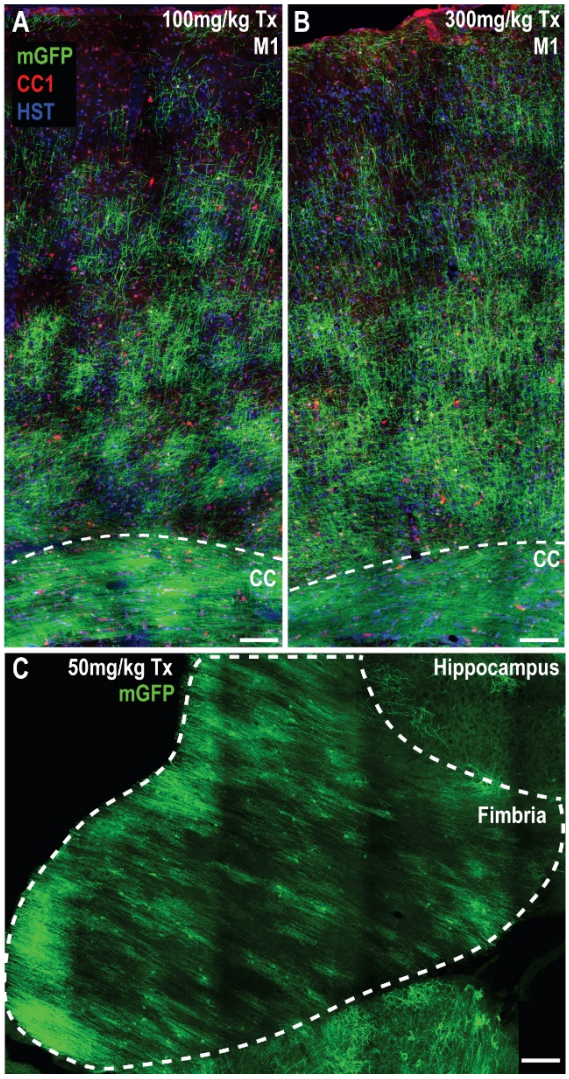

Figure S1. Mature, myelinating oligodendrocytes become mGFP-labeled following Tamoxifen administration to *Plp-CreER :: Tau-mGFP* transgenic mice

A) Confocal image of M1 and the CC of a P80+15 *Plp-CreER :: Tau-mGFP* mouse that received a single 100mg/kg dose of Tamoxifen (Tx), with its brain subsequently being stained to detect GFP (green), the oligodendrocyte marker CC1 (red) and Hoescht 33342 (blue). **B**) Confocal image of M1 and the CC of a P80+15 *Plp-CreER :: Tau-mGFP* mouse that received a single 300mg/kg dose of Tamoxifen, with its brain being stained to detect GFP (green), CC1 (red) and Hoescht 33342 (blue). In mice that received only 100mg/kg of Tamoxifen, it was possible to discern individual GFP-labeled $CC1^+$ oligodendrocytes and their associated myelin internodes in the cortical layers. It was not possible to distinguish individual GFP-labeled $CC1^+$ oligodendrocytes and their associated internodes within the CC of *Plp-CreER ::Tau-mGFP* mice that received 100 or 300 mg/kg Tamoxifen. **C**) Confocal image of the hippocampal fimbria of a P60+15 *Plp-CreER :: Tau-mGFP* mouse that received a single 50mg/kg dose of Tx. It was not possible to reliably attribute $mGFP^+$ internodes to a single oligodendrocyte within the fimbria. Scale bars represent 100µm (A-B) or 75µm (C). Related to Figures 1 & 3

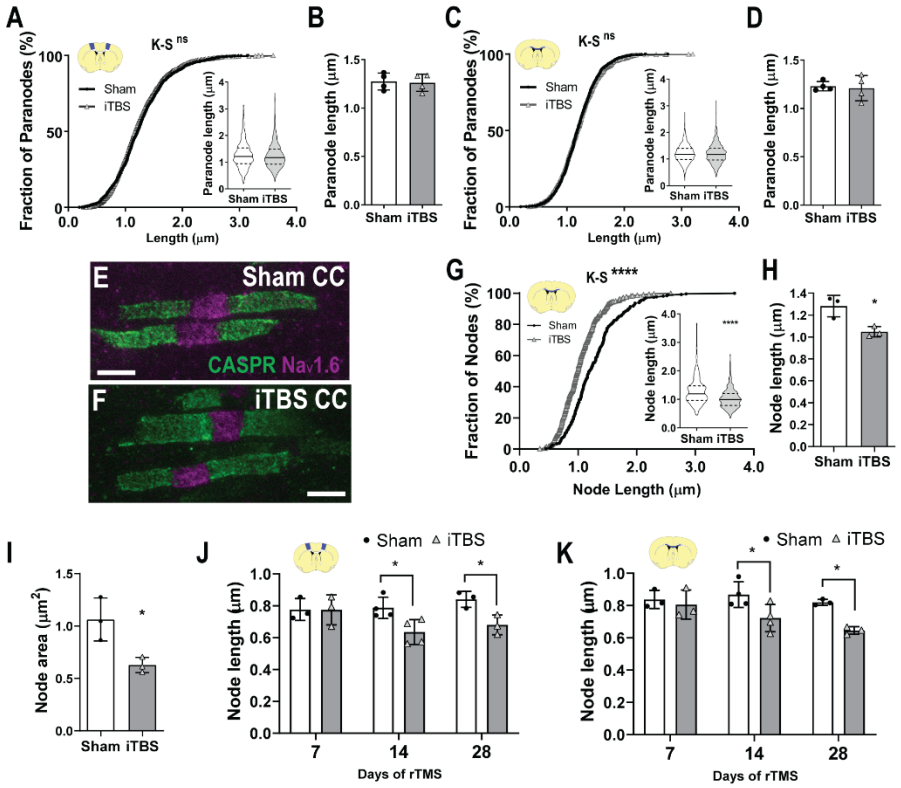

Figure S2. iTBS does not alter paranode length.

A) Cumulative paranode length distribution in M1 [1268 sham (black circles) and 1335 iTBS (gray triangles) paranodes; K-S test, K-S D= 0.053, p=0.054; Inset, violin plot of paranode length, MWU test p=0.06]. **B**) Average M1 paranode length per individual sham (white) and iTBS (gray) treated mouse [n=4 mice per group, t-test, t=0.20, p=0.84]. **C**) Cumulative paranode length distribution in the CC [1099 sham and 1181 iTBS paranodes; K-S test, K-S D=0.03, p=0.65; Inset, violin plot of paranode length, MWU test p=0.73] of mice receiving sham-stimulation and iTBS. **D**) Average CC paranode length per sham and iTBS stimulated animal [n=4 per group, t-test, t=0.28, p=0.78]. **E-F**) Representative STED image of nodes of Ranvier ($Na_v1.6$; magenta) and paranodes (CASPR; green) from the CC of sham (**E**) and iTBS (**F**) mice. **G**) Cumulative distribution plot of node length in the STED imaged CC of sham and iTBS treated mice [269 sham and 325 iTBS nodes; K-S test, K-S D=0.27, p<0.0001; Inset, violin plot of paranode length, MWU test p<0.0001]. **H**) Average CC node length (STED imaged) per sham and iTBS treated animal [n=3 per group, t-test, t=3.73, p=0.02]. I) Average cross-sectional area of CC nodes per sham and iTBS animal [n=3 per group, t-test, t=3.45, p=0.02]. **J**) Average node length per animal in M1 following 7, 14 or 28 days of sham or iTBS [2-way ANOVA: interaction F(2,14)=2.42, p=0.12; duration F(2,14)=1.56, p=0.24; treatment F(2,14)=10.55, p=0.005]. **K**) Average node length per animal in the CC following 7, 14 or 28 days of sham or iTBS [2-way ANOVA: interaction F(2,14)=1.88, p=0.18; duration F(2,14)=2.73, p=0.09; treatment F(2,14)=14.55, p=0.002]. Violin plots show the median (solid line) and interquartile range (dashed lines). Bars show mean ± SD. *p<0.05 by t-test (**H-I**) or Bonferroni's post-test (**J-K**). Scale bars = 1μm. Note: 14-day data shown panels **J-K** are also shown in related Figure 2.

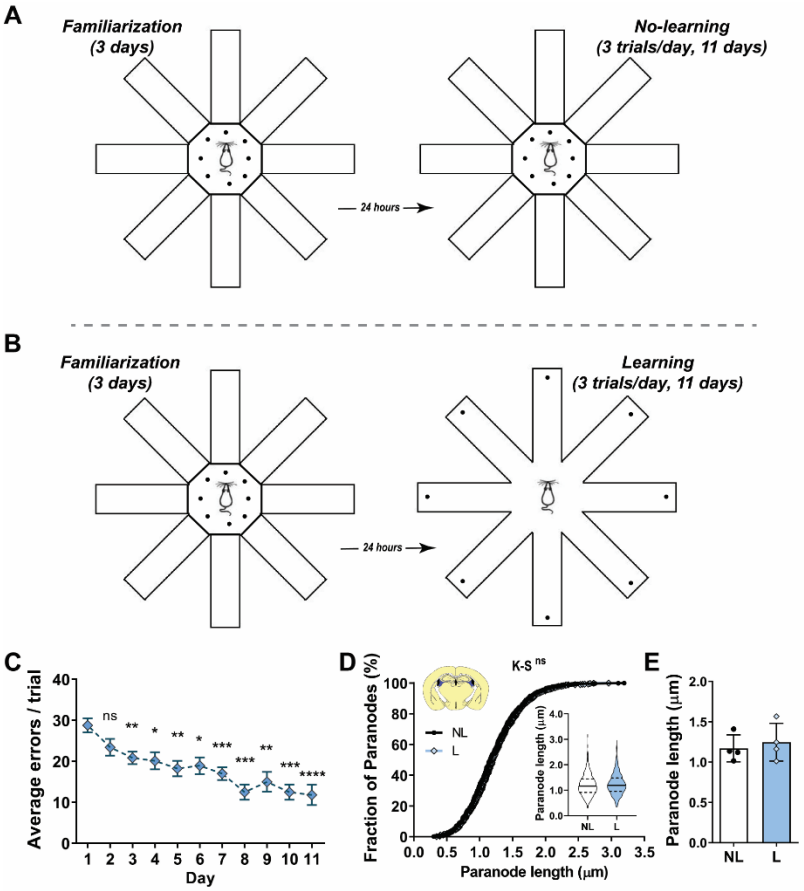

Figure S3. Spatial learning does not change paranode length in the fimbria.

A) Schematic outlining the radial arm maze (RAM) procedure during the first 3 days of familiarization to the maze and over the following 11 days for no-learning control mice. Each dot represents a piece of Froot Loop® that was used as a food reward stimulus and placed in the center of the maze for each trial over a total of 14 days. **B**) Schematic outlining the procedure during the familarization phase (first 3 days) and learning phase (last 11 days) of the RAM spatial learning task. Each dot represents a piece of Froot Loop® that was used as a food reward stimulus. Food rewards were placed in the center of the maze during the familiarization phase, but a single piece of Froot Loop® was placed at the end of each arm during each trial of the learning phase. Mice learned to enter each arm and consume the single food reward only once during a trial, with repeated entries into an arm in which the food reward was already consumed being recorded as a recall error. **C**) Quantification of the average number of errors made across 3 trials each day by mice learning the RAM task. Over the course of 11 days the mice progressively learned the task and made fewer errors [RM one-way ANOVA with Bonferroni post-test: $F(4.65, 46.51)=19.37$, $p<0.0001$. Mean ± SEM for n=11 mice]. **D**) Cumulative paranode length distribution in the fimbria of mice that underwent no-learning (NL; black circles) or learning (L; blue diamonds) in the RAM **[**831 no-learning and 881 learning paranodes; K-S test, K-S D=0.059, p=0.096; Inset, violin plot of paranode length, MWU test p=0.058]. **E**) Average fimbria paranode length in NL (white) and L (blue) mice [n=4 mice per group, t-test, t=0.52, p=0.61]. Violin plots show the median (solid line) and interquartile range (dashed lines). Bars show mean ± SD. *p<0.05, **p<0.01, ***p<0.001, ****p<0.0001 compared to day 1 by Bonferroni post-test. Related to Figure 3.

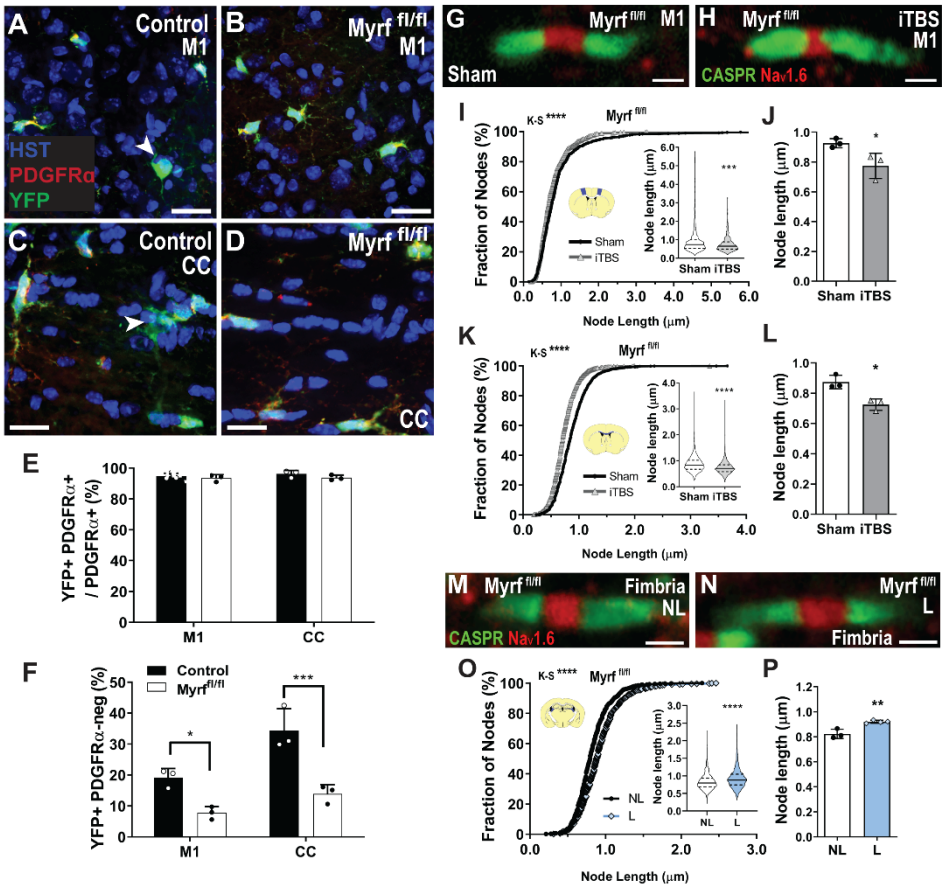

Figure S4. Preventing oligodendrogenesis does not affect activity-induced nodal plasticity.

Tamoxifen was administered to P60 control (*Pdgfrα-CreER^{TM}:: Rosa26-YFP*) and Myrf$^{fl/fl}$ (*Pdgfrα-CreER^{TM} :: Rosa26-YFP :: Myrf $^{fl/fl}$*) mice to turn on expression of YFP in OPCs and allow the lineage tracing of their progeny. Tamoxifen also resulted in the conditional deletion of *Myrf* from adult OPCs. **A-D**) Compressed confocal image from M1 (**A-B**) and CC (**C-D**) of P60+30 control (**A, C**) and Myrf$^{fl/fl}$ (**B, D**) mice stained to detect PDGFRα (red), YFP (green) and Hoescht 33342 (blue). **E**) The proportion of PDGFRα^{+} OPCs that underwent recombination and become YFP-labeled in M1 and the CC of P60+30 control (black bars, white circles) and Myrf$^{fl/fl}$ (white bars, black circles) mice [2-way ANOVA: region F(1,8)=0.57, p=0.46, gene F(1,8)=2.49, p=0.15, interaction F(1,8)=0.33, p=0.57. Mean ± SD. n=3 mice per group]. **F**) Quantification of the proportion of PDGFRα-neg YFP-labeled (and OLIG2^{+}) newly differentiated oligodendrocytes in M1 and the CC [2-way ANOVA with Bonferroni post-test: region F(1,8)=19.86, p=0.002, gene F(1,8)=43.56, p=0.0002, interaction F(1,8)=3.56, p=0.095]. **G-H**) Node of Ranvier (Na$_v$1.6; red) in M1 of Myrf$^{fl/fl}$ mice after 14 days of sham-stimulation (**G**) or iTBS (**H**). **I-J**) Cumulative node length distribution in M1 [**I**; 620 sham (black circles) and 727 iTBS (gray triangles) nodes; Kolmogorov-Smirnov (K-S) D=0.12, p<0.0001; inset violin plot of node length, Mann Whitney U (MWU) test, p<0.0001] and average node length per sham (white) or iTBS (gray) treated mice (**J**); [n=3 mice per group, t-test, t=2.93, p=0.04]. **K-L**) Cumulative node length distribution in the CC (**K**) [1903 sham and 1670 iTBS nodes; K-S D=0.17, p<0.0001; inset violin plot of node length, MWU test, p<0.0001] and the average node length per animal (**L**) of Myrf$^{fl/fl}$ mice after sham-stimulation or iTBS [n=3 mice per group, t-test, t=4.453, p=0.01]. **M-N**) Node of Ranvier (Na$_v$1.6; red) in the fimbria of Myrf$^{fl/fl}$ no-learning (NL; **M**) and learning (L; **N**) mouse after RAM. **O-P**) Cumulative node length distribution in the fimbria [**O**; 635 no-learning (black circles) and 718 learning (blue diamonds) nodes; Kolmogorov-Smirnov (K-S) D=0.19, p<0.0001; inset violin plot of node length, Mann Whitney U (MWU) test, p<0.0001] and average node length per no-learning (NL; white, n=3) or learning (L; blue, n=4) mouse (**P**); [t-test, t=4.99, p=0.0041]. Violin plots denote the median (solid line) and interquartile range (dashed lines). Arrows indicate newborn oligodendrocytes. *p<0.05, ***p<0.001, ****p<0.0001. Scale bars represent 13μm (A-D), 1μm (G-H, M-N). Related to Figure 4.

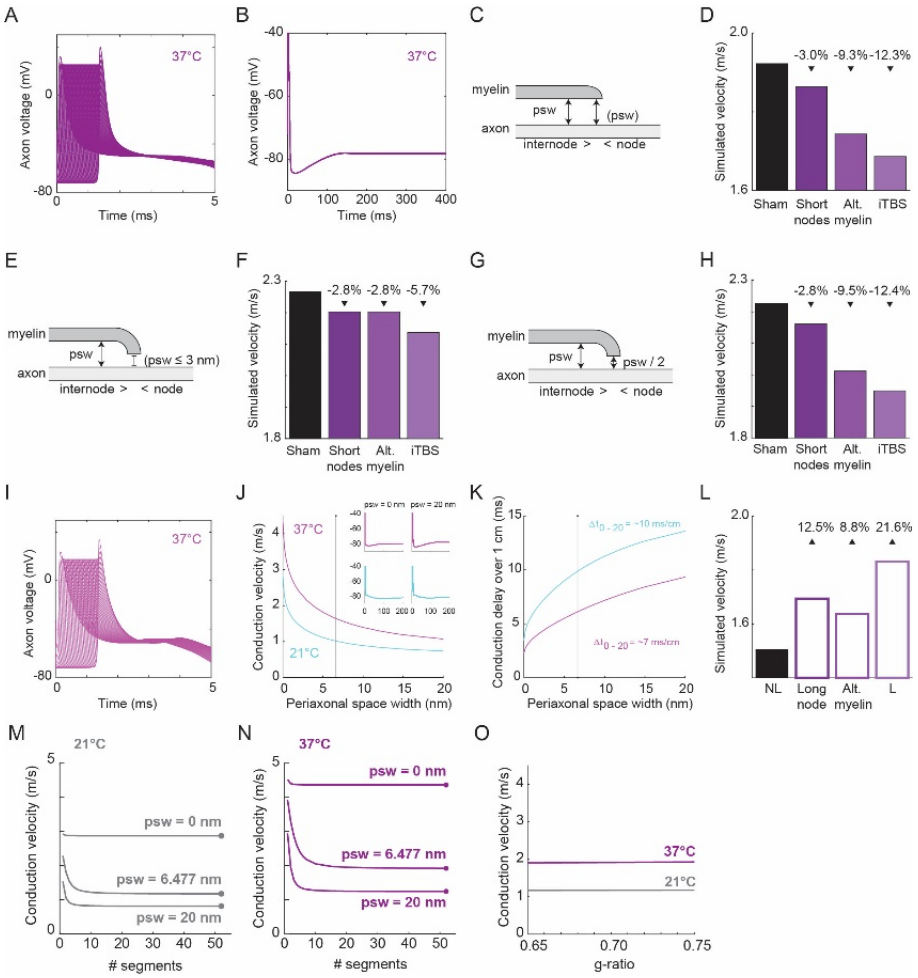

Figure S5. Mathematical simulation of conduction in myelinated CNS axons.

A) Action potentials simulated at consecutive nodes in the CC at 37°C. **B**) The extended time-course of action potentials generated by the model at 37°C. **C**) Schematic showing model parameters in which periaxonal space width (*psw*) at the paranode is uniform to internode *psw*. **D**) Predicted conduction velocity of a sham stimulated (white) axon versus an axon with either the node length shortened, the periaxonal space widened or both (iTBS, shades of magenta) using the model depicted in (C). **E**) Schematic showing model parameters in which *psw* at the paranode is set to ≤ 3nm. **F**) Predicted conduction velocity of a sham stimulated axon versus an axon with either the node length shortened, periaxonal space widened or both (iTBS) using the model depicted in (E). **G**) Schematic showing model parameters in which *psw* at the paranode is set to half the width in the internode. **H**) Predicted conduction velocity of a sham stimulated axon versus an axon with either the node length shortened, periaxonal space widened or both (iTBS) using the model depicted in (G). **I**) Action potentials simulated at consecutive nodes in the fimbria at 37°C. **J**) Simulated conduction velocity of fimbria axons relative to periaxonal space width (*psw*) at 37°C (light magenta) and 21°C (cyan), solid line indicates average *psw* following iTBS and insets show action potential waveforms at the extremities of the tested range (*psw* = 0 or 20nm) at 21°C and 37°C. **K**) Conduction delay over 1cm relative to *psw* in the fimbria at 21°C and 37°C. **L**) Predicted conduction velocity of a no-learning (NL) control axon within the fimbria at 37°C (white) versus an axon with either longer nodes, a narrower periaxonal space or both (learning, L). Controls for the convergence of conduction velocity in mathematical simulations (**M**, **N** and **O**). Conduction velocity simulations were run at 21°C (**M**) or 37°C (**N**), using a periaxonal space width (*psw*) within the physiological range measured in the study (6.477nm) or at two extremes (*psw* = 0nm and *psw* = 20nm), and with an increasing number of segments per internode. In all scenarios, using N = 52 segments (finishing dots), ensured that a stable prediction of the conduction velocity was reached irrespective of the width of the periaxonal space. **O**) Changing the g-ratio alone over the range tested here (from 0.65 to 0.75), without changing the periaxonal space width or the number of myelin wraps, has little to no effect on the conduction velocity (calculated for sham cortical axons). Changing the g-ratio from 0.6888 to 0.724 (see Table S1) amounts to a change in conduction velocity of -0.5% at 21°C (gray) and -0.9% at 37°C (magenta). Related to Figure 5.

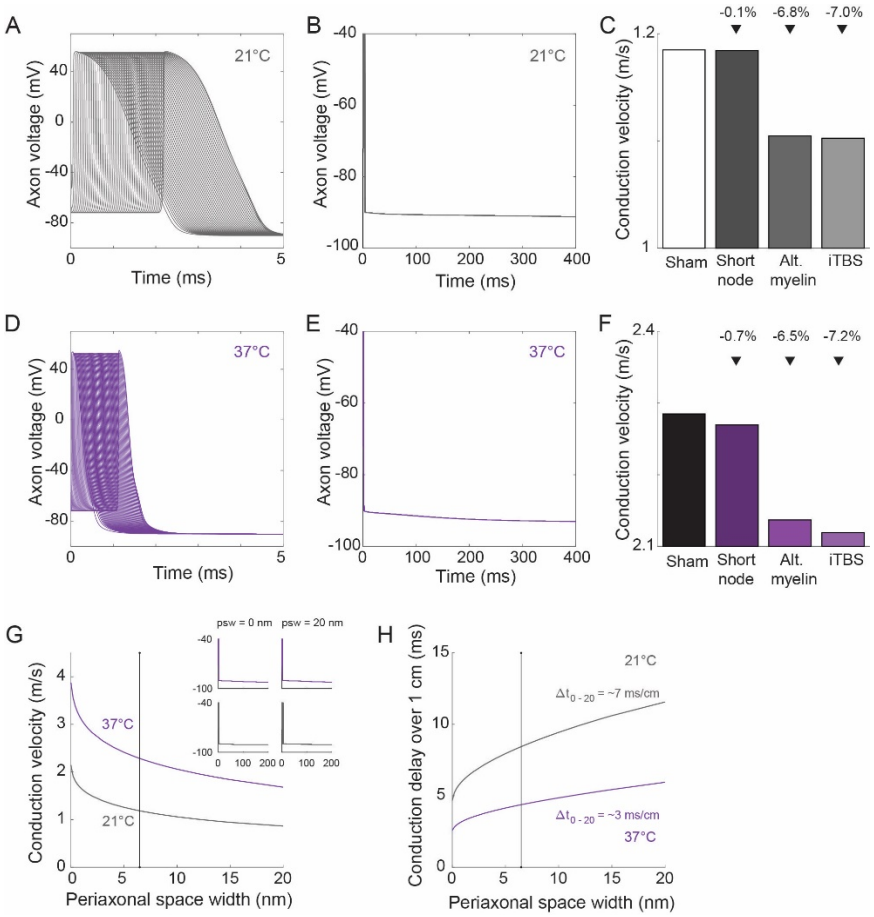

Figure S6. Mathematical simulation of conduction in myelinated CNS axons with axonal and periaxonal space resistivities as in Cohen *et al.* (2020).

A) Action potentials simulated at consecutive callosal nodes at 21°C. **B**) Extended time course of action potentials generated by the model. **C**) Predicted conduction velocity of sham a sham stimulated (white) axon versus an axon with either node length shortened, the periaxonal space widened or both (iTBS) at 21°C. **D**) Action potentials simulated at consecutive callosal nodes at 37°C. **E**) Extended time course of action potentials generated by the model. **F**) Predicted conduction velocity of a sham stimulated (black) axon versus an axon with either node length shortened, the periaxonal space widened or both (iTBS) at 37°C. **G**) Simulated conduction velocity of callosal axons relative to periaxonal space width (*psw*) at 37°C (magenta) and 21°C (gray). Vertical line indicates average *psw* following sham stimulation (*psw* = 6.477nm) and insets show action potential waveforms at the extremities of the tested range (*psw* = 0 or 20nm) at 21°C and 37°C. **H**) Conduction delay over 1cm relative to *psw* at 21°C and 37°C (8.5ms at 21°C, and 5.2ms at 37°C for *psw* = 6.477nm). **Note that in each of these simulations (**A-H**), axonal resistivity = 1.5 Ω•m; periaxonal space resistivity = 0.54 Ω•m, as per the values reported in (Cohen *et al.*, 2020). To achieve similar action potential conduction velocity to our earlier simulations (**Figure 6, S5**) g_{Naf} and g_K were adapted so that g_{Naf} = 550 mS/mm^2 and g_K = 24 mS/mm^2. Related to Figure 6 and S5.

Table S1. Parameters used in computational simulations of action potential conduction velocity. Related to Figure 6, S5 and S6. See STAR methods for mathematical modelling.

Parameter		Sham	Short nodes*	Alt. myelin*	iTBS*	No-Learning	Long nodes*	Alt. myelin*	Learning *
Internode length	µm	50.32				38.89			
Axon diameter	µm	0.5894				0.5938			
Node length	µm	0.8364	0.7735		0.7735	0.6644	0.8668		0.8668
RMP	mV	-72				-72			
Node capacitance	µF/cm^2	0.9				0.9			
Internode capacitance	µF/cm^2	0.9				0.9			
Internode leak conductance (g_L)	mS/mm^2	0.1				0.1			
E_L	mV	-84				-84			
Axoplasmic resistivity	Ω•m	0.7				0.7			
Periaxonal resistivity	Ω•m	0.7				0.7			
Periaxonal space width	nm	6.477		8.487	8.487	8.265		6.709	6.709
g-ratio		0.724		0.6888	0.6888	0.7009		0.7419	0.7419
Number lamellae		7				7			
Myelin membrane capacitance	µF/cm^2	0.9				0.9			
Myelin membrane conductance	mS/mm^2	1				1			
g_{Naf}	mS/mm^2	50				50			
g_{Nap}	mS/mm^2	0.05				0.05			
g_K	mS/mm^2	0.8				0.8			

* Only detailed if different from the control (sham/no-learning) condition.